2019

Computational Study of Water Desalination Using Forward Osmosis

Ahmed Mohammed Alshwairekh
Lehigh University, shoierkh@qu.edu.sa

Recommended Citation

Alshwairekh, Ahmed Mohammed, "Computational Study of Water Desalination Using Forward Osmosis" (2019). *Theses and Dissertations*. 4339.
https://preserve.lehigh.edu/etd/4339

Computational Study of Water Desalination Using Forward Osmosis

by

Ahmed Mohammed Alshwairekh

Presented to the Graduate and Research Committee
of Lehigh University
in Candidacy for the Degree of
Doctor of Philosophy

in
Mechanical Engineering

Lehigh University
January 2019

SAMPLE DISSERTATION SIGNATURE SHEET

Approved and recommended for acceptance as a dissertation in partial fulfillment of the requirements for the degree of Doctor of Philosophy.

Date

Dissertation Director: Dr. Alparslan Oztekin

Accepted Date

Committee Members:

Committee Chair: Dr. Alparslan Oztekin

Dr. Jacob Kazakia

Dr. Edmund Webb

Dr. Xuanhong Cheng

ACKNOWLEDGMENT

I would like to express my greatest and upmost appreciation to my beloved mother Badryah, for all the prayers and the encouragement that she has given me since the day I was born. I also pray for my father god bless his soul, as he passed away during my graduate studies. I know he would have been so proud of his son's achievement. I also would like to express my great appreciation and gratitude to my wife Fatemah, for all the sacrifice she has given for me during my graduate studies. I'm in dept for her my entire life.

As for my mentor, Professor Alparslan Oztekin, I cannot find the word to describe my feelings for you. You have shown me the way to a new world, the world of academic research. Thank you for all your guidance and wisdom. Thank you for being patient with me during my Ph.D. journey. I couldn't have done any of this without you professor, thank you.

I also would like to thank my Ph.D. committee members, Professor Jacob Kazakia, Professor Edmund Webb, and Professor Xuanhong Cheng for their support and effort in my Ph.D. journey.

Contents:

List of Tables

List of Figures

NOMENCLATURE

A	**pure water permeability**	$m(s\ Pa)^{-1}$
B	**solute permeation coefficient**	$m\ s^{-1}$
C	**solute concentration**	$kg\ m^{-3}$
c	**solute mass fraction**	$kg_{solute}\ kg_{solvent}^{-1}$
D_{AB}	**Solute diffusion coefficient**	$m^2\ s^{1-}$
d_h	**hydraulic diameter**	m
ε	**porous layer porosity**	-
h	**feed and draw channel height**	m
J_w	**water flux**	$kg\ m^{-2}\ s^{-1}$
J_s	**reverse solute flux**	$kg\ m^{-2}\ s^{-1}$
K	**solute resistivity coefficient**	$s\ m^{-1}$
μ	**fluid viscosity**	$Pa\ s$
p	**pressure**	Pa
π	**osmotic pressure coefficient**	Pa
Re	**Reynolds number**	-
t_s	**Porous layer thickness**	m
τ	**tortuosity of porous layer**	-
ρ	**density of fluid**	$kg\ m^{-3}$
U	**Velocity vector**	$m\ s^{-1}$
$\overline{u}$	**average inlet velocity**	$m\ s^{-1}$
x y z	**Cartesian coordinates**	**m**
Subscripts		
dB	**draw bulk**	
fB	**feed bulk**	
f	**feed solution**	
d	**draw solution**	
c	**corrugation**	
e	**Flat channel**	

Abstract

Forward Osmosis is a natural phenomenon that takes places across a semi-permeable membrane when there is a concentration difference across the membrane. Pure water permeates to the highly concentrated channel until the concentration across the membrane equilibrates. In water desalination applications, the same principle is applied. Spiral-wound membrane, flat sheet, or hollow fiber module are typical configurations in forward osmosis desalination modules. The application of water desalination using forward osmosis requires the existence of two channels separated by a suitable forward osmosis membrane. Sea or Brackish water is introduced in one side while the other side has a suitable draw solution. The concentration of the draw solution must possess several properties for optimum performance. The vital property is that the draw solution should have a concentration greater than the sea or the brackish water. The forward osmosis membrane consists of an active dense layer and a porous support layer. The membrane should be designed to have high pure water permeability with a low solute permeation coefficient and a low structural parameter. Low values of the structural parameter ensure that the effect of the internal dilutive concentration polarization is neglected.

The process of water permeation in a forward osmosis membrane module has been modeled using computational fluid dynamic simulations. The local variation of the water flux along the membrane surface as a function of the local concentration of both the feed and the draw channels was calculated. The permeation of the water flux causes the concentration in the feed channel to increase as the salt start to accumulate over the

membrane surface. While the concentration of the draw solution is diluted as the water mixes with the draw solution.

In the simulations with a flat membrane and no mixing promoters, a laminar model was used. In the model, Navier-Stokes equations along with a mass transport equation were used to model the flow and the variation of the concentration inside the channels. The flow rate was varied to study the effect of the concentration boundary layer growth in forward osmosis membrane systems. Also, the thickness of the porous support layer was varied. The results indicate that increasing the flow rate indeed improved the water flux by reducing the growth of the concentration boundary layer. The presence of the porous support layer drastically reduces the performance of the system because of the high level of the internal dilutive concentration polarization (active layer facing feed solution orientation). It is important to reduce the thickness of the porous support layer, increase the porosity or improve the tortuosity of the porous support layer. The optimum solution is to remove the porous support layer completely.

Corrugating the membrane should mix the feed and the draw solutions near the membrane surface. The membrane was corrugated in a chevron manner. Four different types of corrugations were considered: (1) a single corrugation where the peak of the corrugation is towards the feed side to avoid fouling; (2). a double membrane corrugation so that both the feed and the draw solutions are mixed; (3) a channel corrugation in which the membrane is left flat: and (4). a combined corrugation in which the double and channel corrugations are combined. In each set of simulations, three Reynolds number were considered giving twelve sets of simulations in total. The $k-\omega$ SST model is utilized to characterize the steady state turbulent structures inside the modules containing corrugations for Re of 300, 800, and 1500. The results indicate that the porous support layer is still reducing the performance of the membrane system even with the introduction of the corrugations. However, there has been improvement in the water flux up to 15% in the combined corrugation case.

The final part of the dissertation research focused on removing the effect of the porous support layer and introducing embedded spacers within the structure of the membrane. Net-type spacers of 45° and three different spacer strand diameters are used. The diameters of the spacer are chosen as $0.1h$, $0.2h$, and $0.3h$. The flow rate was changed so that Re is 300, 800, and 1500. The results indicate that the case with $D = 0.3h$ and Re = 300 had the best performance.

Chapter 1: Introduction

Water shortages is a serious problem that is facing the world [1]. Most countries around the world are trying to overcome the problems of water shortages through several ways such as increasing people awareness, water reuse, and desalination [2]. Water desalination is one of the promising ways of having enough water supplies. However, it requires a tremendous supply of energy. It is reported that half of the domestic oil in the middle east goes to water purification purposes [3]. There are several methods of producing pure water from sea or brackish water resources and are discussed in details in [4–6].

Water desalination is considered as one of the most used methods of producing clean and fresh water. As the world's population continues to grow, the demand on clean water will grow with it. Freshwater resources are scares and cannot able to supply the world population with enough water. Also, freshwater resources are not equally distributed around the world. Some parts of the world suffer from the lack of fresh water and have severe droughts throughout the year. The only feasible way of getting water in abundant quantities to these regions is by using desalination methods. Thermal desalination was one of the early methods of water desalination. However, due to the high cost of operation and environmental impact the use of thermal desalination is limited to only some parts of the world. Saudi Arabia and Kuwait employ mostly thermal desalination since fossil fuel sources are abundant in these countries. On the other hand, membrane systems have a more economic option to water desalination. Different methods of membrane systems are used. Reverse Osmosis (RO) is a well-documented desalination method and a commercially available option. In RO, a hydraulic pressure is applied across a semi-permeable membrane to induce a selective mass transfer through the membrane which permits water molecules to the permeate channel and leaving behind salt and other particles. More information about RO can be found in Ref [7–10].

Other methods of water desalination can be considered such as Forward Osmosis (FO). FO systems rely on the existence of osmotic pressure which is induced by the concentration difference of sea or brackish water and a draw solution. A semi-permeable membrane is used to physically separate the two solutions and to separate water from salt and particulate in the feed channel by the action of the net osmotic pressure difference. Sea or brackish water is introduced in the feed side, with a suitable draw solution in the draw channel. An osmotic pressure starts to develop across the semi-permeable membrane causing mass transfer to occur. As seawater gets drawn to the draw solution, salt starts to accumulate on the membrane surface in the feed channel which causes what is known as concentrative external concentration polarization (CECP). At the same time, pure water starts to dilute the draw solution on the draw side of the porous layer support of the membrane. This leads to dilutive internal concentration polarization (DICP) phenomena. As pure water is further transferred to the bulk of the draw channel, dilutive external concentration polarization (DCEP) occurs, as illustrated in Figure 1. The combination of CECP, DICP, and DECP drastically reduces the net osmotic pressure difference in the system [11]. Mitigation of concentration polarizations in these separation module is focus of recent studies in this field.

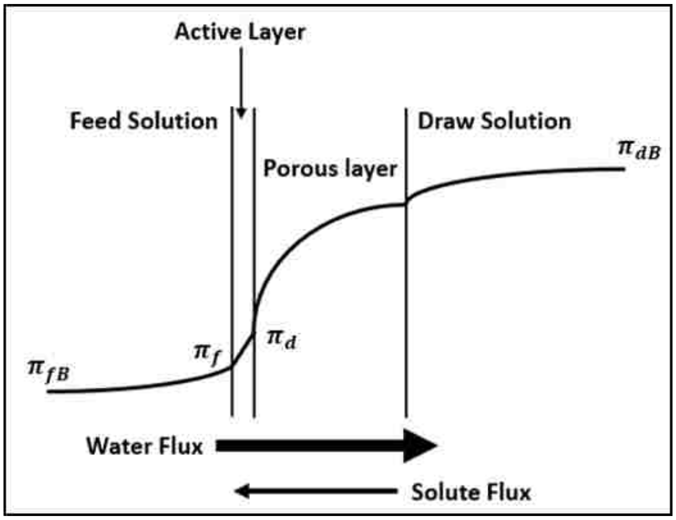

Figure 1. *Schematic of An Asymmetric Membrane*

Literature Review

Several researchers have studied FO as a desalination tool by using Spiral Wound Membranes (SWM). Gruber et al. [12] developed a CFD model and conducted several numerical experiments to study the effect of cross-flow velocity, the net osmotic pressure difference and membrane slip velocity on water flux. They concluded that increasing the cross-flow velocity increases the water flux as it reduces the concentration polarization (CP) on the membrane from both sides. Hawari et al. [13] conducted several experiments to study the effect of different operating conditions such as membrane orientation, solution temperature, and flow rate on the membrane water flux. The results showed that the water flux increased with increasing flow rate of both feed and draw solutions. The water flux also increased as temperature was increased from 20 °C to 26 °C. They also observed that DICP became worse with increasing flow rate. Zhang et al. [14] experimentally investigated the effect of spacers location on the water flux enhancement with two different membrane orientations. They found that by placing the spacer near the membrane in both channels in FO mode, both CECP and DICP were decreased.

Other investigators have studied the effect of flow field disruption on the membrane flux performance. Anqi et al. [15,16] developed a CFD model in a reverse osmosis desalination module to study the effect of spacers on reducing concentration polarization. Their results suggest that spacers can mitigate the severity of concentration polarization and hence water flux increases. Usta et al. [17] developed a CFD model to study reverse osmosis desalination module containing a corrugated membrane. The corrugations on the membrane surface serve as micro-mixers and reduce the severity of concentration polarization. The results indicate that membrane corrugations enhanced membrane performance at all flow rates.

Other researchers have studied the effect of the porous layer on the membrane flux performance. Wei et al. [18] developed a thin film composite polyamide FO membrane with a tailored support layer. They reported a high-water flux with the new membrane at high draw concentration. Han et al. [19] designed a novel thin film composite membrane specifically for FO desalination. The reported membrane flux was high only at a high osmotic pressure and reduced to nearly half when lowering the osmotic pressure difference.

Several researchers [10–13] have used spacers in FO modules to promote mixing in the feed and draw streams. The spacers also work as extra mechanical support for the membrane. Gruber et al. [20] used an open-source CFD simulation to optimize FO and RO systems. Several parameters were investigated to study their effect on the membrane system performance. All the parameters were related to the geometry of the FO module such as including several inlets, changing the angle of the inlet, spacer's type and configurations. Their results indicate that including several inlets and varying the angles didn't have any significant i in the water flux. The inclusion of spacers increased the water flux in the model. Also, the shape and orientation of spacers had a direct effect on water flux. The triangular spacer gave the highest flux. Park et al. [21] numerically studied the effect of spacer inclusion in FO modules. Concentration polarization was used as an index for characterizing the performance of FO system. They varied the concentration difference across the semi-permeable membrane and recorded the values of water flux with calculating the concentration polarization. They concluded that spacers managed to reduce the concentration polarization. Liu et al. [22] conducted an experimental study in FO membrane systems. They studied the rejection of antibiotic from wastewater treatment plants using FO membrane. Their experiment focused on adding spacers in the feed channel. The spacers increased the rejection of the antibiotics since spacers induced turbulence that disturbed the boundary layer next to the membrane. Linares et al. [23] experimentally evaluated the effect of spacer thicknesses on mitigating fouling over the membrane.. Their results suggest that thicker spacers are better for mitigating fouling over the membrane.

Several researchers [17,24,25] have used corrugated membranes as micro-mixers to mitigate external CP and enhance system performance. Corrugated membranes have been previously researched in membrane systems, but extensive literature search didn’t reveal any membrane corrugation in FO modules. The use of corrugation should enhance FO systems as it disrupts the concentration boundary layer over the membrane surface. Tzanetakis et al. [24] experimentally investigated the process of salt splitting using electrohydrolysis technique. In the experiment they used a flow cell composed of two compartments where the membrane is in the middle. Two types of ceramic membrane were used, the first was flat membrane and the second was corrugated. The corrugated membrane had a 57% increase in surface area compared to the flat membrane. Their results indicated that corrugation increased the current efficiency and improved the achievable base concentration. Scott et al. [25] experimentally studied a microfiltration process to purify a water-in-oil emulsion with a corrugated membrane. The effect of flow rate, feed channel height, transmembrane pressure and the angle of membrane corrugation on flux rate were given. Their results indicate that increasing the flow rate and decreasing the feed channel height yielded better performance since the water flux increased because of shear rate increase on membrane surface. The effect of membrane corrugation resulted in a better performance as water flux increased with a reduction in concentration polarization. Membrane corrugation promoted turbulence near the membrane. The corrugation angles of 45° and 90° gave water flux enhancements of 100 and 160% compared with the flat membrane. Also, the 45° and 90° corrugation angles reduced the energy consumption by 80 and 88%, respectively. Usta et al. [17] conducted a CFD study on a corrugated membrane in a RO module. The membrane used in their study was corrugated in a rectangular and triangular chevron manner. In their study, they used flow rates that correspond to Reynolds numbers of 100, 400 and 1000. Their results indicated that using triangular chevron corrugation enhanced the membrane performance in all flow rates used as the water flux increased and the concentration polarization was alleviated.

Several researchers attempted to reduce the level of the ICP in FO membranes by modifying the structure of the porous support layer. Song et al. [26] developed a new nanocomposite FO membrane that uses a Nano-support layer. The new membrane had low values of tortuosity, high porosity, and thin porous support layer. These features give the permeate water a direct path to the draw channel and for the draw solution to reach the membrane active layer surface. The structural parameter of the NC-FO membrane was low. The water flux under FO experimental setup gave high water flux which indicates that the ICP level was reduced. Puguan et al. [27] synthesized a nanofiber thin film composite membrane with a Crosslinked electrospun polyvinyl alcohol nanofiber as porous support layer. The aim of designing their new membrane was to make the porous support layer hydrophilic, highly porous and poses low tortuosity. The structural parameter of the new membrane was low, and the water flux did not improve compared to Song et al. [26] with the same concentration difference across the membrane. Ghanbari et al. [28] developed a new membrane that has a hydrophilic nanotubes inside the porous support layer. The membrane showed high water permeability and low reverse solute flux. They attribute the high-water flux obtained with this membrane to the low structural parameter compared with other thin-film composite membranes. Kuang et al. [29] used calcium carbonate nanoparticles to prepare the porous support layer. Then hydrochloric acid was used to etch the calcium carbonate nanoparticles to increase the porosity of the support layer. The results showed low values of structural parameter and high porosity within the porous layer. Bui et al.[30] fabricated a new membrane by incorporating mesoporous silica nanoparticles into the nanofiber porous support layer of the membrane. This technique aims to increase the selectivity and to reduce the level of the ICP. Their membrane showed remarkable flux increase especially with pressure retarded osmosis mode.

From the studies discussed above, it is evident that the existence of the porous support layer hinders any advancement in FO and PRO systems. Most research was focused on reducing the porous support layer thickness, increasing the porosity, and having better tortuosity for low ICP. The optimum solution is to remove the porous support layer completely. The complete removal of the porous support layer is an engineering challenge. Recently, Li et al. [31] developed a new membrane with only a dense active layer without the need for any support. The developed membrane had very low values of structural parameter where they can be assumed zero. In their membrane, the actual osmotic pressure equals the ideal osmotic pressure within regular thin film composite membranes with sponge like porous support layers. The pure water permeability of the new membrane, however, was very low. The water flux achieved is still low, and the pure water permeability needs to be improved while maintaining the mechanical strength for better utilization of such membranes.

Chapter 2 is devoted to the mathematical modelling of a forward osmosis desalination system. Chapter 3 is a detailed study for the effect of the porous support layer in forward osmosis membranes. Chapter 4 shows the results for the effect of the channel and the membrane corrugations in forward osmosis desalination modules. Chapter 5 shows the results for the concept of embedded spacers in forward osmosis membranes systems. Chapter 6 has all the concluding remarks concerning the results presented in the dissertation.

Chapter 2: Mathematical Model

The equations governing the flow in the feed and draw channels are the conservation of mass and momentum equations. The flow is considered as incompressible. However, density is taken as a function of solute mass fraction. Thus, the conservation of mass can be written as:

$$\nabla.(\rho\mathbf{U}) = 0 \tag{1}$$

With steady state conditions and variable physical properties, the momentum equation is:

$$\nabla.(\rho\mathbf{U}\mathbf{U}) = \nabla.[\mu(\nabla\mathbf{U} + \nabla\mathbf{U}^T)] - \nabla p \tag{2}$$

The mass transport equation in the feed and draw channels is described as:

$$\nabla.(\rho\mathbf{U}c) - \nabla.(\rho D_{AB}\nabla c) = 0 \tag{3}$$

Several researchers [17–21] conducted CFD simulations in membrane systems containing turbulence promoters using the turbulent model $k-\omega$ shear stress transport (SST). We employed the $k-\omega$ SST turbulence model to characterize the steady state turbulent structures induced by the presence of the embedded spacers. The SST k-ω turbulence momentum equation is written as

$$\frac{\partial\rho\mathbf{U}}{\partial t} + \nabla.(\rho\mathbf{U}\mathbf{U}) = \nabla.[(\mu + \mu_t)(\nabla\mathbf{U} + \nabla\mathbf{U}^T)] - \nabla p \tag{4}$$

Here, μ_t is the eddy viscosity and it can be written as $\mu_t = \rho\frac{a_1 k}{\max(a_1\omega, SF_2)}$. The turbulent kinetic energy k and the specific dissipation rate ω, are given as

$$\frac{\partial(\rho k)}{\partial t}+u_i\frac{\partial(\rho k)}{\partial x_i}=\tau_{ij}\frac{\partial u_i}{\partial x_j}-\beta^*\rho\omega k+\frac{\partial}{\partial x_j}\left[(\mu+\sigma_{k1}\mu_t)\frac{\partial k}{\partial x_j}\right] \tag{5}$$

$$\frac{\partial(\rho\omega)}{\partial t}+u_i\frac{\partial(\rho\omega)}{\partial x_i}=\frac{\gamma}{\nu_t}\tau_{ij}\frac{\partial u_i}{\partial x_j}-\beta\rho\omega^2+\frac{\partial}{\partial x_j}\left[(\mu+\sigma_\omega\mu_t)\frac{\partial\omega}{\partial x_j}\right] +2\rho(1-F_1)\sigma_{\omega2}\frac{1}{\omega}\frac{\partial k}{\partial x_j}\frac{\partial\omega}{\partial x_j} \tag{6}$$

The model parameters and the constants that appeared in equations (7-9) are given in full details in [22]. Also, S is the vorticity magnitude and $(a_1,\beta,\beta^*,\sigma_{k1},\sigma_\omega,\sigma_{\omega2}\ and\ \gamma)$, (F_1,F_2) are closure coefficients and blending functions, respectively.

Density, viscosity and diffusion coefficient are function of solute mass fraction only. They are given as empirical expressions of NaCl at 25 °C [32].

$$\rho=997.1+694\ c \tag{7}$$

$$\mu=0.89\times10^{-3}(1+1.63\ c) \tag{8}$$

$$D_{AB}=\begin{cases}1.61\times10^{-9}(1-14\ c) & for\ c<0.006\\ 1.45\times10^{-9} & for\ c>0.006\end{cases} \tag{9}$$

In the present work, the membrane is modeled as a functional permeable surface with zero thickness. The no-slip boundary condition is imposed. The water flux through the membrane can be modeled using the solution-diffusion model as [7]:

$$J_w=A\left(\pi_d-\pi_f\right) \tag{10}$$

In equation (10), A is the pure water permeability, π_d is the osmotic pressure at the interface between the porous layer and the active layer of the membrane, π_f is the osmotic pressure at the active layer of the membrane in the feed side. The osmotic pressure of NaCl is obtained from the empirical expression as [32]

$$\pi = 805.1 \times 10^5\, c \qquad (11)$$

The flux model presented in Eq. 10 neglects the effect of the porous layer of the membrane and overestimates the water flux. The porous layer of the membrane has an adverse effect on the performance of the membrane since it gives rise to DICP in FO. To better model the water flux through an FO membrane, a modified flux equation proposed by Loeb et al. [33] is used:

$$J_w = \frac{1}{K} ln\left(\frac{B + A\pi_d}{B + |J_w| + A\pi_f}\right) \qquad (12)$$

In Eq. 12, B is the solute permeation coefficient. The water flux equation takes into account mass and momentum transport inside the porous layer and how solute diffuses inside the porous layer through the solute resistivity coefficient K defined as [34]:

$$K = \frac{t_s \tau}{D_{AB} \varepsilon} \qquad (13)$$

Eq 12 is an implicit equation. A ridder solver was used to solve this equation within Fluent. A user-defined function was written based on the open source model developed by Gruber [12] in his work.

Here t_s is the support layer thickness, ε the porosity. τ the tortuosity defined as [35]:

$$\tau = 1 - 0.8 \ln(\varepsilon) \qquad (14)$$

The solute reverse flux through the active layer of the membrane is modeled as:

$$J_s = -B\left(C_d - C_f\right) \tag{15}$$

The negative sign indicates that the solute flux is opposite of water flux.

At both inlets of the feed and draw channels, the boundary conditions are:

$$\begin{cases} c = c_{in} \\ u = 6\bar{u}\dfrac{y}{h}\left(1 - \dfrac{y}{h}\right) \\ v = 0 \\ w = 0 \end{cases} \tag{16}$$

$\bar{u}$ is the average inlet velocity in both channels. y is the vertical distance. h is the channel height. It is to be noted that the inlet concentration of the draw channel must always be higher than the feed concentration. At impermeable walls:

$$\begin{cases} no\ slip - no\ penetration \\ \dfrac{\partial c}{\partial y} = 0 \end{cases} \tag{17}$$

At the outlet of the feed and the draw channels, the pressure is set to zero and the concentration is set to a zero gradient.

At the surface of the membrane on both sides, the boundary conditions imposed on the concentration and velocity fields, respectively are:

$$\begin{cases} -\rho D_{AB}\dfrac{\partial c}{\partial y} + \rho c J_w = J_s \\ v_w = \dfrac{1}{K} ln\left(\dfrac{B + A\pi_d}{B + |J_w| + A\pi_f}\right) \\ u = 0 \quad and \quad w = 0 \end{cases} \tag{18}$$

v_w is the local water permeating at the membrane surface, u and w are the velocity components at x and z direction.

Chapter 3: Parametric Study - Effect of Porous Layer Thickness and Operation Parameters

Computational fluid dynamics (CFD) simulations are conducted to study the transport phenomena in spiral wound membranes (SWM) within a Forward Osmosis (FO) module. The effect of the porous layer on the membrane performance is examined. Simulations are prepared for three different porous layer thicknesses by having the porous layer facing the draw channel, a mode known as AL-FS (active layer facing feed solution). In the current study, Reynolds number range from 2 to 500 is considered. The Navier-Stokes and the mass transport equations are used to obtain the velocity, pressure and concentration fields in the flow channels. The local osmotic pressure and the membrane properties are used to calculate the water permeation over the membrane surface. The membrane is considered as a semipermeable functional surface of zero thickness. The effect of the porous layer is included in the flux model, but the flow and concentration fields in the porous layer are not resolved. The results suggest that increasing the streamwise velocity decreases the level of the external concentration polarization on both sides of the membrane which in turn leads to higher water flux through the membrane. Also, the existence of the porous layer reduced the membrane performance. The water flux didn’t improve much with increasing streamwise velocity at the same porous layer thickness. The suction velocity over the membrane starts at a high value at the inlet of the draw channel and decreases until reaching the outlet of the draw channel then it starts to increase slightly from the effect of the inlet of feed solution. Moreover, by increasing the net osmotic pressure difference, the water flux exhibited a non-linear increase.

Mesh Study and Validation

In this work, FO membrane was modeled using a modified form of the solution-diffusion model as it is given in chapter 2, mathematical modeling in Eq. 18. To validate the membrane boundary conditions, another set of simulations were conducted and compared with a published experimental study conducted by Yip et al. [36]. In their work, several new membranes were manufactured and tested under different conditions. The membranes were made from a selective polyamide active layer and a polysulfone support layer with a polyester nonwoven fabric. The porous layer exhibited a finger like pores for better membrane performance. In conducting FO desalination experiments, the draw solution used was NaCl of concentration of 1.5 M and the feed solution was pure water.

To validate the membrane boundary conditions, an empty channel was created, and the Reynolds number of the simulation was matched with the experimental conditions. A laminar model was used since Reynolds number was set to 1147 without any turbulence promoters. The inlet mass fraction of the draw channel was set to 0.09 while the feed mass fraction was set to 0 to model pure water. The pure water membrane permeability, A was set as $3.18 \times 10^{-12} \frac{m}{s\,Pa}$ and the solute permeation coefficient B, was set as $1.46 \times 10^{-7} \frac{m}{s}$. The structural parameter of the membrane was calculated based on Eq. 10 from Appendix A. Different values of the structural membrane were given, each value represents a membrane. A total number of six simulations were conducted to ensure the validity of the membrane boundary conditions.

Average water flux values along the membrane were used to compare the experimental cases and the simulated ones. The results are tabulated and presented in the Table 2. The values of the water flux are reported in units of $\frac{L}{m^2h}$. Membranes considered in this study are made of the same materials. The only difference between them is the way the support layer is manufactured. The structural parameter can be used to represent each membrane as

$$S = \frac{t_s\tau}{\varepsilon}$$

where t_s is the membrane thickness, τ is the tortuosity of the membrane and ε is the porosity of the porous support layer. The average thickness of all the membranes used is reported as $95.9 \pm 12.6\ \mu m$.

Table 1. *Experimental and simulated results of average water flux over the membrane and the error in the boundary conditions*

	TFC-1	TFC-2	TFC-3	TFC-4	TFC-5	TFC-6
Experimental	19.51	16.81	17.57	17.95	18.93	18.17
Simulation	19.73	17.35	17.79	18.5	18.6	18.01
Deviation	1.13%	3.21%	1.25%	3.06	-1.74	-0.88%

As it can be seen from Table 1, the boundary conditions used in the simulations can predict the reported experimental values in the literature. The highest error was only 3.21% while the lowest error is -0.88%. The boundary conditions might over estimate or under estimate the reported experimental values of the water flux. However, in either case the error is small, and the boundary conditions can be considered as an accurate model for FO desalination.

The current study investigates the effects of porous layer thickness on the FO membrane separation process. To achieve this, the Navier-Stokes and mass transport equations were solved for different concentration of draw solution and different thicknesses of porous layer (PL) at Re $= 100$ and 500 in the three-dimensional feed and draw channels.

The mesh optimization test was conducted on three different structured meshes: M1, M2, and M3 which corresponds to 1 million, 2 million and 4 million meshes, respectively. The mesh near the membrane surface was refined so that the first layer thickness is 5 μm which is required to capture the effect of concentration polarization [9]. The simulations reveal that 2 million cells were enough to obtain spatial convergence. Figure 2a shows the streamwise velocity component at x/h = 20 for both channels. Figure 2b shows the concentration variation of the draw and feed solutions vertically at x/h = 20. The dotted vertical line at y = 1 mm represents the membrane surface. Figure 2c shows the concentration variation of feed solution along the surface of the membrane at z/h = 2.5. Figure 2d shows the concentration variation of draw solution along the surface of the membrane at z/h = 2.5. In Figures 2a and 2b, the profiles matched perfectly. However, Figures 2c and 2d show a slight deviation between the profiles in the different meshes. This deviation is clear in Figure 2d since the variation of draw concentration along the membrane is higher than the feed concentration.

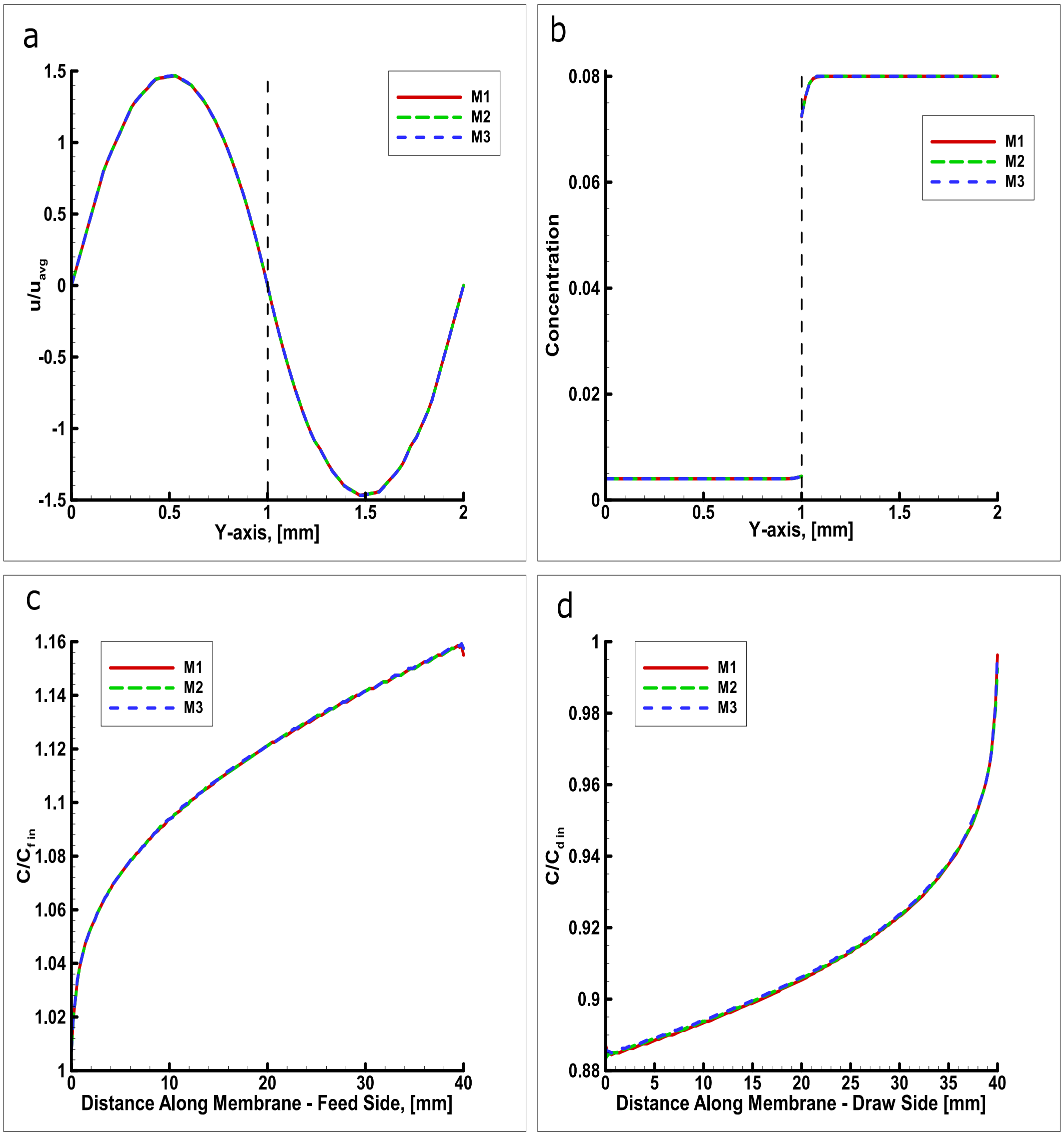

[redacted]

Results

Results are presented in dimensionless quantities. The concentration of the draw and feed are normalized based on the inlet concentration of draw and feed, respectively. The velocity is normalized based on the average inlet velocity. The water flux through the membrane is normalized as $J_w/(\Delta\pi\ A)$.

Figure 3 shows the development of the concentration boundary layer (BL) over the membrane surface on the draw side. The concentration is normalized by the draw inlet concentration and rendered at the middle of the channel at z/h = 2.5. The development of the BL is due to DECP which is caused by the transfer of pure water from the feed to the draw side. The BL continues to grow as the flow continues downstream of the draw channel. The development of the BL has an adverse effect on the performance of the membrane separation process as it reduces the net osmotic driving force. The BL size is a function of the streamwise velocity and flow pattern inside the channel. It is desirable to increase the streamwise velocity to reduce the BL thickness as it is evident from Figure 5. Moreover, the addition of spacers will disrupt the BL growth and enhance the system performance [16], however; this is outside the scope of the current study.

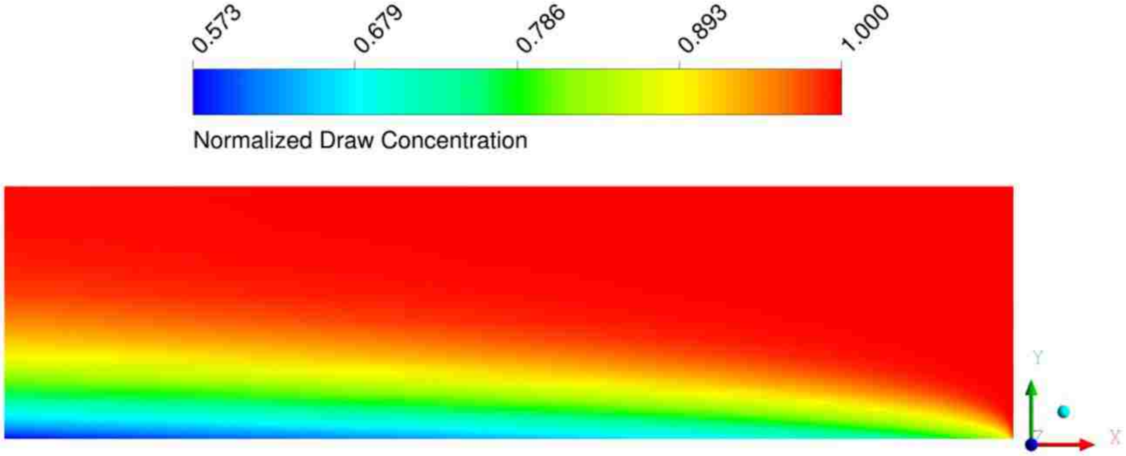

Figure 3. *contours of the normalized concentration in a plane in the draw channel. The lower edge represents the membrane surface.*

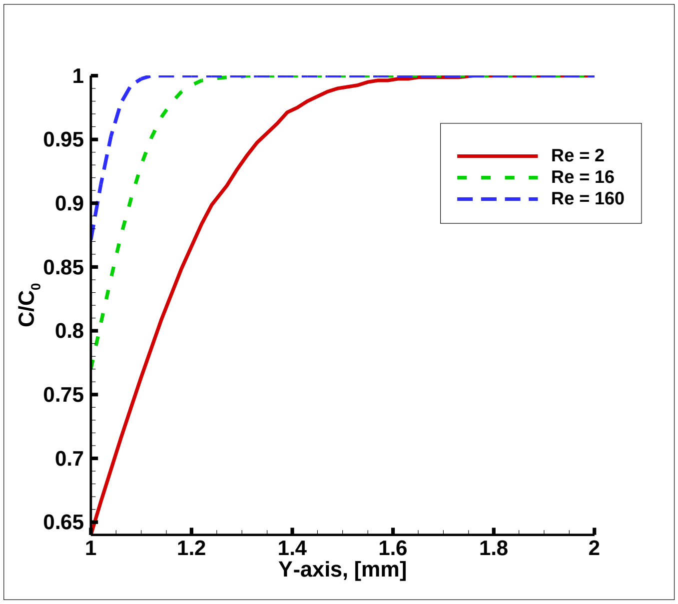

Figure 4. *Normalized concentration curves at the middle of the draw channel for three different Reynolds numbers.*

Figure 4 shows a similar trend in the feed channel. The concentration is normalized by the feed inlet concentration and rendered at the middle of the channel at z/h = 2.5. As the water permeates to the draw side, salt concentration starts to accumulate over the membrane surface in the feed side causing a BL growth that reduces the net osmotic pressure difference. This phenomenon is known as CECP, and it is easily managed by making the flow turbulent. Figure 6 shows that the thickness of the boundary layer in the feed channel is much less than that on the draw side.

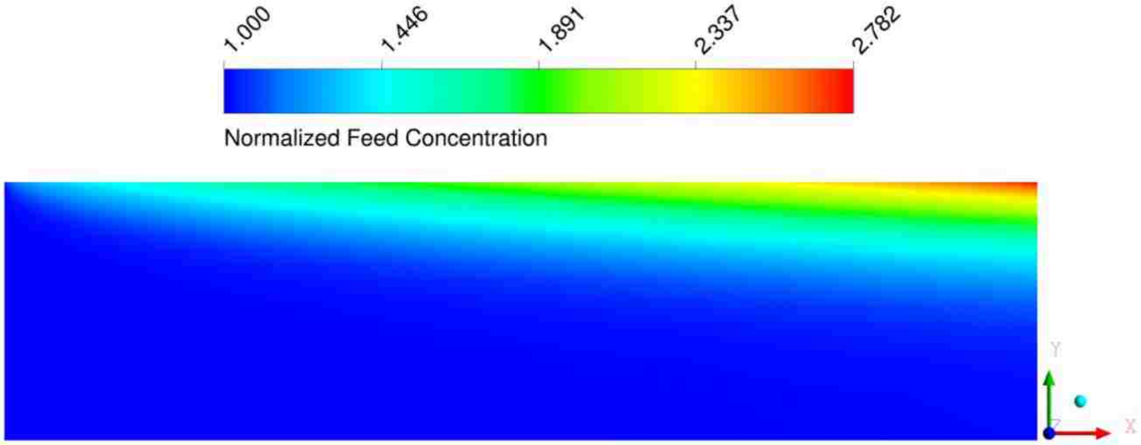

Figure 5. *Contours of the normalized concentration in a plane in the feed channel. The top edge represents the membrane surface.*

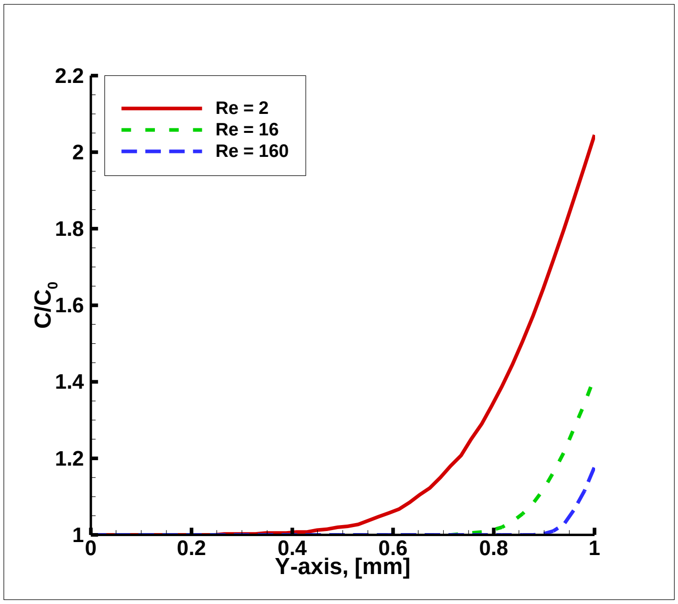

Figure 6. *Normalized concentration curves at the middle of the feed channel for three different Reynolds numbers*

Figure 7 shows normalized profiles of the water flux along the membrane at the draw side. The water flux is higher at the inlet of the draw channel. The flux starts to decrease slightly as the flow continues down the channel. This reduction in water flux is due to the fact that DECP is developing along the channel as it is depicted in Figure 3a. When the flow reaches the draw outlet, a slight increase in the water flux is noticed. This increase is attributed to the less concentrated brackish water entering from the feed side since the flow is countercurrent.

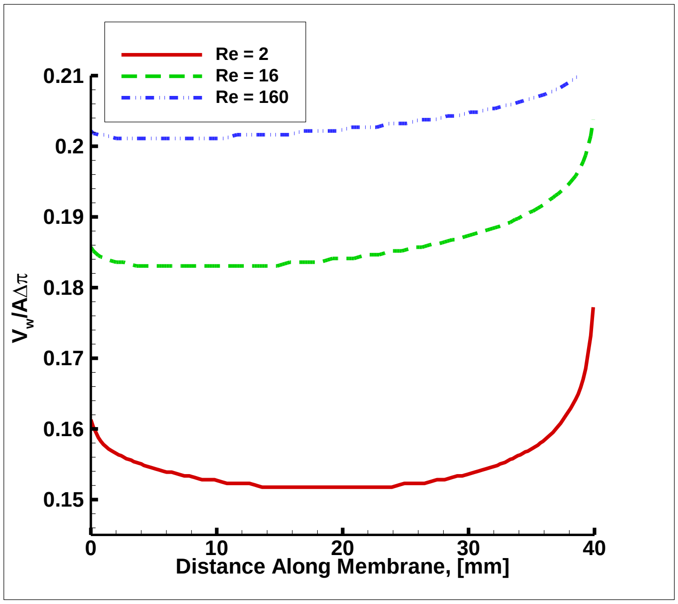

Figure 7. *Normalized water flux profiles along the membrane surface for three different Reynolds numbers*

Effect of Porous Layer Thickness

Recently, researchers started to focus on designing new and improved FO membranes. Several design parameters can affect the membrane design. The PL thickness is such a parameter. It is expected that by decreasing the PL thickness the water flux through the membrane will be enhanced and DICP phenomena will decrease as it is evident from equation 6. Gray et al. [37] conducted several experiments and calculated the resistant to solute diffusion coefficient inside the PL and concluded that it needs to be as small as possible for better FO performance.

Table 2. *Averaged water flux data at different porous layer thicknesses and Reynolds number.*

	$J_w(kg\ m^{-2}\ h^{-1})$	
$t_s(\mu m)$	Re = 100	Re = 500
50	8.044	8.339
80	6.261	6.434
110	5.172	5.290

A series of numerical experiments were conducted to study the effect of PL thickness in FO processes. The PL thickness was varied as 50, 80 and 110 μm for Re of 100 and 500. Table 2 shows the averaged results of the numerical experiments. The net osmotic pressure difference in all simulations was set to 2.1 MPa. The porosity of the membrane was set to 0.22.

As it is expected, when porous layer thickness increases the water flux decreases. The water flux decreased from 8.044 to 6.261 $kg\ m^{-2}\ h^{-1}$ from 50 μm to 80 μm at Re = 100 which correspond to a 28% decrease in water flux. This reduction in water flux is mainly due to the prolonged pure water diffusion inside the PL. As the PL thickness increases from 50 μm to 110 μm the water flux reduces by an amount of 56%.

At higher streamwise velocities, either DECP or CECP can be mitigated. This is evident in the results shown in table 2. The water flux values at higher Reynolds number had improved slightly at the same PL thickness. At PL thickness of 50, 80 and 110 μm the water flux enhancement due to the increase in streamwise velocity was 4%, 3% and 2%, respectively. As the PL thickness increases the PL becomes more dominant and flow manipulation will not play any role in water flux enhancement.

Effect of Draw concentration

The driving force in FO membrane systems is the net osmotic pressure across the membrane which is a function of the feed and draw solution concentration. Naturally, as the concentration difference increases the water flux should increase accordingly. Eq. 16 suggests that the increase in water flux has a linear relationship with net osmotic pressure difference. However, Eq. 18 suggest otherwise.

In this series of simulations, the feed concentration was set to $c_f = 0.004$ which correspond to brackish water salinity. The draw concentration was varied from c_d= 0.01 up to 0.09. The thickness of the membrane used was $50\ \mu m$. This range of concentration difference will induce a pressure difference across the membrane up to 7 MPa. In each simulation, the averaged water flux through the membrane is recorded. Figure 8 shows the water flux variation with different osmotic pressure difference across the membrane. The non-linear relationship of water flux with osmotic pressure is due to the effect of DICP which reduces the effective driving force over the active layer of the membrane.

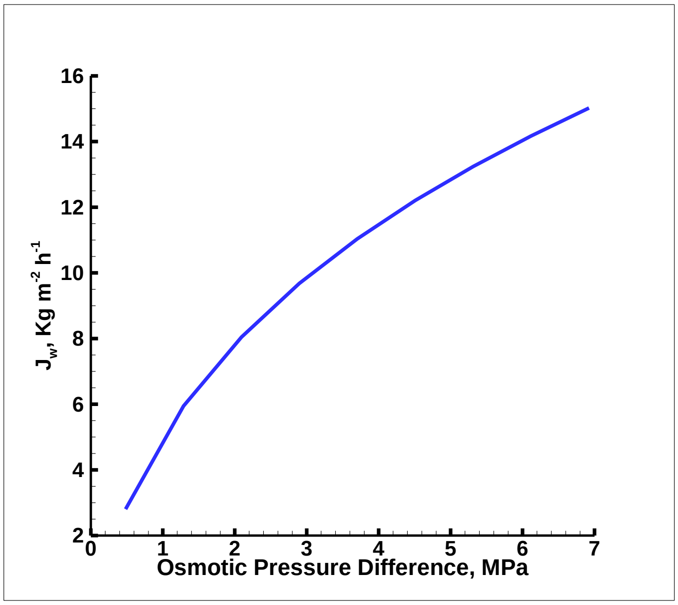

Figure 8. *Water flux values over a wide range of osmotic pressure difference*

Conclusion

A series of three-dimensional steady-state simulations were conducted to study FO membrane systems including the effect of the porous layer. Navier-Stokes and mass transport equations are solved by means of finite volume method. A modified version of the solution-diffusion model was used for estimating the water flux through the membrane with porous layer. Accurate flow fields and concentration of feed and draw solutions were obtained. This study highlights the importance of the porous layer in FO membrane systems. A great deal of care should be given to the design of FO membranes for better FO performance.

The results showed the development of the concentration and dilutive concentration polarization boundary layers. It has shown that with small porous layer thicknesses, the streamwise velocity has a direct effect on increasing the performance of FO systems. As the flow rate increases, the boundary layer thickness decreases which increase the net osmotic pressure difference across the membrane.

The value of the water flux permeating in the draw channel is highest at the draw inlet and decreases as the flow progress down the draw channel. Near the draw outlet, the water flux starts to increase slightly from the effect of the feed channel inlet.

The porous layer thickness has a direct effect on the performance of FO systems. As the porous layer thickness decreases, the water flux increases. The water flux reduces by 56% as the PL thickness increase from 50 to 110 μm. Increasing the flow rate at high PL thicknesses will not have any significant influence on water flux enhancement.

The difference between draw and feed concentration translates to the driving force in FO processes. As the draw concertation increases, the water flux increase in a non-linear fashion. As the water flux through the porous layer increases, the DICP becomes significant and that reduces the effective driving force in the active layer.

Chapter 4: Effect of Membrane and channel Corrugation

Computational fluid dynamics simulations were used to model the effect of the membrane and channel corrugation in forward osmosis desalination systems. The modified solution-diffusion model was used to predict the water flux through the membrane by including the effect of the porous support layer. The flux model couples the concentration of the feed and draw solution to predict the water permeation rate. The distribution of the water flux, concentrative and dilutive concentration polarization and shear stress were monitored over the surface of the membrane. The laminar model was used in the module with no corrugation, and $k-\omega$ SST turbulence model was used in the modules consisting of corrugations for Re = 300, 800 and 1500. The flux model was validated quantitatively against existing experimental work with membrane systems containing net-type spacers. The results indicate that single membrane corrugation and channel corrugation are more effective in mitigating the external concentrative and dilutive concentration polarizations and alleviating the potential fouling than the double and combined membrane corrugations. Nearly 15% increase in water permeation rate was obtained with the combined corrugation case. The coefficient of performance suggests that the single and double corrugation cases at Re = 300 had the best performance.

Numerical Model, Convergence, and Validation

In conducting the simulations for membrane systems containing corrugated membranes, several geometries were developed. The outer dimensions of the computational domain are equal for all cases. An alternation of channel and membrane corrugation was used. The corrugation was inspired from the study conducted by Usta et al. [17]. In their work, they used two types of corrugation, triangular and rectangular corrugation in a reverse osmosis desalination module. In forward osmosis, the application of membrane corrugation should have similar improvement as in reverse osmosis. However, there is one main difference between applying corrugation in forward osmosis and reverse osmosis. In forward osmosis, two streams needs to be considered, the feed and draw solutions while in reverse osmosis only the feed solution is of interest. This difference makes the application of membrane corrugation much more involved in forward osmosis than reverse osmosis. The main reason for membrane corrugation is to induce mixing in the feed and draw channels to alleviate external CP. Different types of corrugation can induce different levels of mixing. Since the corrugations are of chevron type over the membrane surface, the flow pattern produced by it will be different in either the feed or draw channels. The corrugation is comprised of eight groups of three consecutive ribs. The ribs are placed 1.1h away from each other in the same group. Also, each group is placed 5h away from any of the neighboring groups. The depth and width of each corrugation was set to 0.2 h. The angle between two chevron ribs is set to 90°. The length and width of the computational domain is 60h and 5h, respectively, where h is the height of each channel. A schematic is shown in Fig. 9.

We first examined the effect of channel corrugation. The bottom of the feed channel and the top of the draw channel are corrugated, as it is shown in Fig. 9 with a single triangular corrugation. The feed solution enters from the left where the draw solution enters from the right which makes the system a counter current flow. The membrane is taken to be straight in the channel corrugation case.

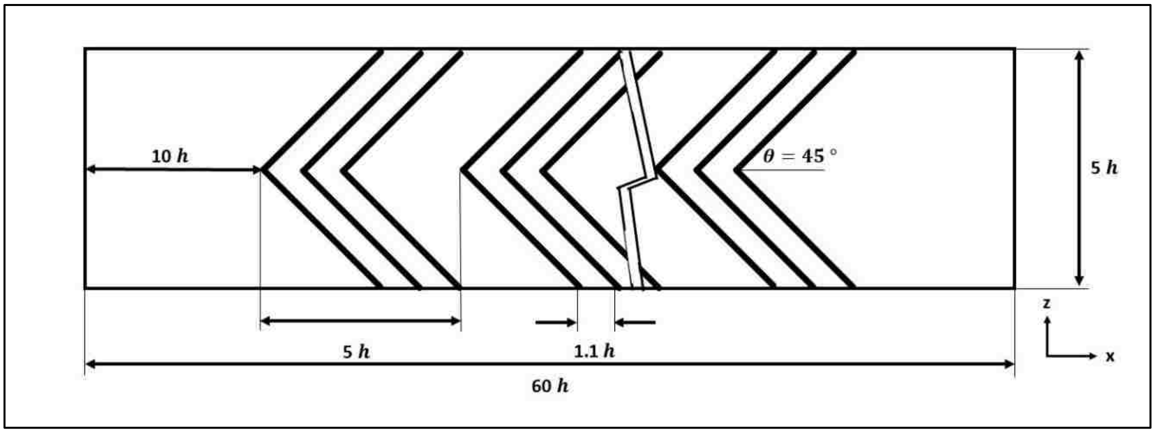

Figure 9. *Top view of a corrugated membrane or channel*

We next examine the effect of membrane corrugation. We consider two geometries consisting of membrane corrugation. For the first geometry, the membrane is to be corrugated in a single triangular corrugation as it is shown in Fig. 10. The peak of the corrugation is chosen to be toward the feed channel. The reason for orienting the peak of the corrugation towards the feed channel is to help mitigate the fouling that might occur due to salt buildup. Even though fouling is not directly modeled in this work, but it is correlated with external concentrative CP.

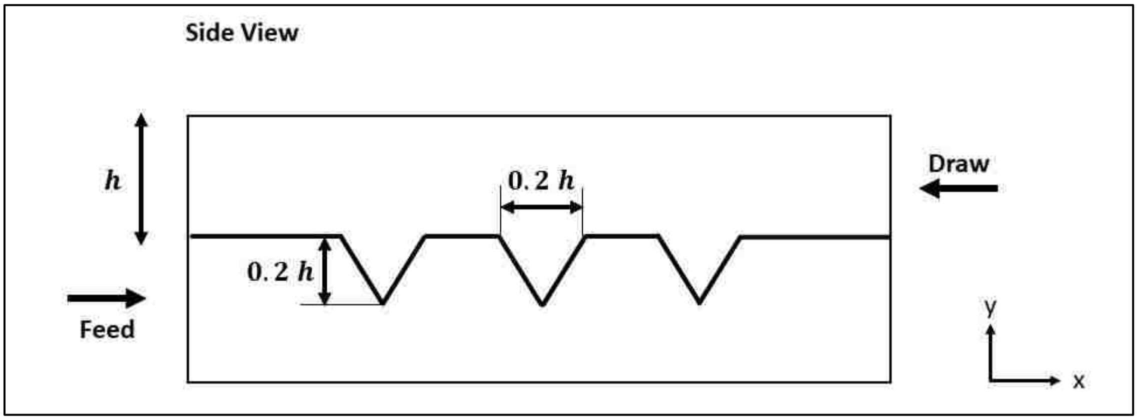

Figure 10. *Side view of a singular triangular membrane corrugation*

For the second geometry, the membrane will be corrugated in a double triangular corrugation. A schematic is shown in Fig. 11. Both channels will have corrugation peaks. Also, both channels will have corrugation dips. This type of corrugation might help in alleviating external CP in both sides because of the double peak arraignment. It might also be prone to fouling inside the dips in the feed channel.

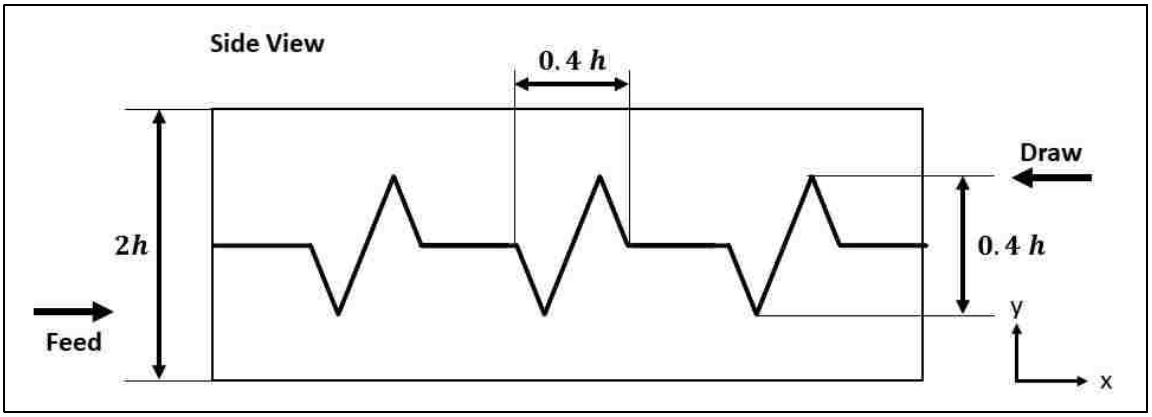

Figure 11. *Side view of a double triangular membrane corrugation*

We last consider the geometry consisting combined channel and double corrugation of membrane. As it was explained earlier, the channel corrugation setup is shown in Fig. 9 and the double corrugation is shown in Fig. 11. By combining these two corrugations, it is expected that the disadvantages of having dips on both sides of the channels are eliminated by the presence of channel corrugation. However, greater pressure loss is expected in this configuration. Table 3 summarizes all geometries used in this work.

Table 3. *A list of simulated cases*

Case	Description	Re		
1	Empty	300	800	1500
2	Channel Corrugation	300	800	1500
3	Single Corrugation	300	800	1500
4	Double Corrugation	300	800	1500
5	Combined Corrugation	300	800	1500

The computational domain was meshed by using Ansys meshing tool. The mesh used was unstructured, and an inflation layer was employed near the membrane surface in both channels. The thickness of the first layer in the mesh near the membrane surface was set to $5\,\mu m$ to capture the external CP in both channels [9]. The total number of mesh elements used was 20 million mesh for all the simulations containing corrugated membranes. This number of mesh elements was the results of a mesh optimization test conducted on the combined case and a Re = 1500. A snap of the mesh showing the double corrugation of the membrane and how the inflation is imposed on the membrane on both sides of the membrane is shown in Fig. 12. Note that the triangular corrugation is not a perfect triangle; a fillet was applied on the tip of the triangle to avoid sharp edges in the mesh.

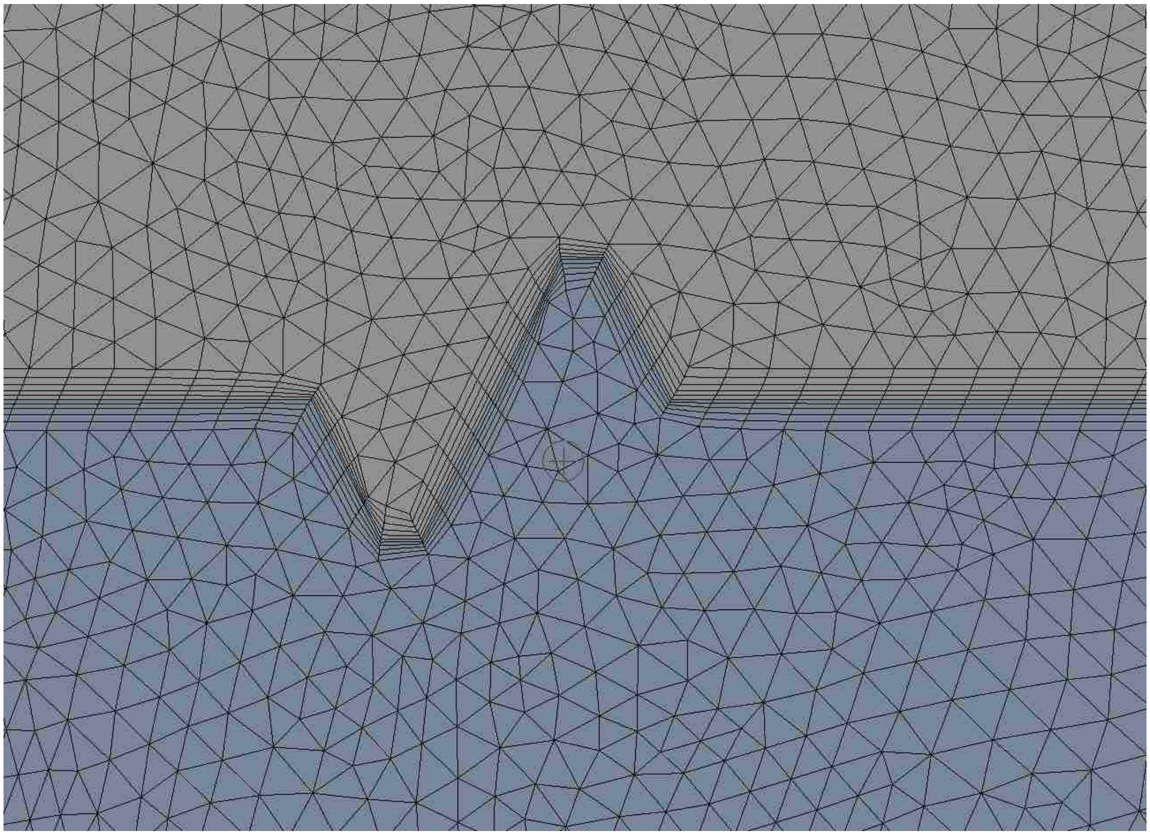

Figure 12. *A snap of the mesh for the double corrugated membrane*

Three different mesh densities were used in the mesh optimization test. The mesh densities were M1, M2 and M3 corresponding to 10, 20 and 40 million elements. The test reveals that a mesh density of 20 million was enough to get a spatial convergence. Fig. 13a shows the normalized stream-wise velocity in the feed channel. The values of the normalized velocity predicted by using M2 and M3 are very similar. Fig. 13b shows the concentration of the feed solution along the membrane surface from the inlet to the outlet. Some deviation is observed in the inlet and outlet regions between the different meshes. In the middle of the channel where corrugations exist the concentration in M2 and M3 are nearly identical. Fig. 13c shows the concentration of the draw solution along the membrane surface in the draw side. Similar trends are seen as it was observed in the feed side. Some deviation is observed at the inlet and outlet regions. The concentration of M2 and M3 in the middle of the channel matches well. The results of mesh study demonstrate that the mesh density M2 is sufficient to ensure spatial convergence. Therefore, M2 mesh was chosen to carry out the rest of the simulations listed in Table 1.

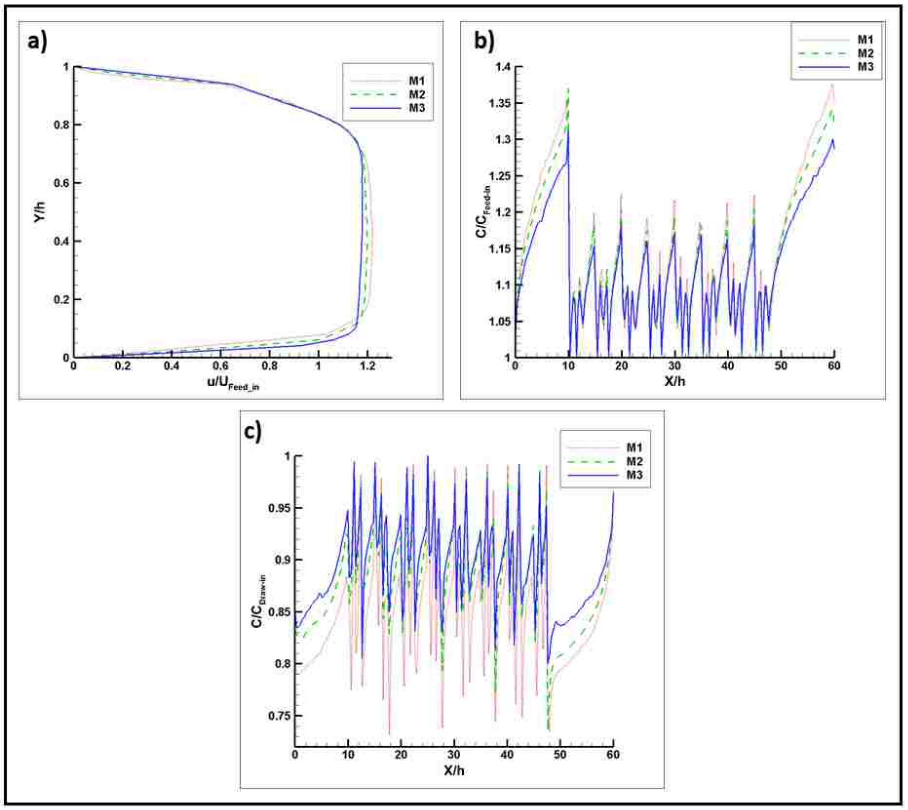

Figure 13. *Profiles of (a) The normalized stream-wise velocity in the feed channel at x/h = 30 and z/h = 25, (b) The normalized concentration along the membrane in the feed channel at z/h = 25 from the inlet to the outlet, (c) The normalized concentration along the membrane in the draw channel at z/h = 25 from the inlet to the outlet.*

To validate the mathematical model and the numerical methods employed, simulations were conducted and predicted results were compared with measurements of the experimental work done by Liang et al. [38]. In their work, they have developed a new membrane with improved water flux. The water flux in the FO mode reached up to 93.6 $L\ m^{-2}h^{-1}$ when the feed solution was deionized water and the draw solution was a sodium chloride aqueous solution with a concentration of 2 $mol\ L^{-1}$. The reason for such high-water flux attained in the experiment is attributed to the low internal concentration polarization and the high membrane permeability. The membrane had similar thickness and porosity values compared with other commercially available thin-film composite membranes. However, the tortuosity of the porous substrate was measured to be 1.1. The lower tortuosity of the membrane yields better water permeation through the membrane and enhanced salt diffusion.

The water permeability for the Vertically Oriented Porous Substrate (VOPS-TFC-1) membrane used in [38] was determined using a pressure-driven test, and it was measured to be $4.71 \pm 0.22\, L\, m^{-2} h^{-1} bar^{-1}$. The salt rejection coefficient (R) was measured to be $93.2 \pm 1.2\%$ for the same membrane. The membrane structural parameter, S, was estimated using Eq. 13 as $99.1 \pm 11.5\, \mu m$, which is smaller than that of typical TFC-FO membranes. The solute permeation coefficient is estimated by Eq 15 using the reported water flux and the salt rejection coefficient. The solute permeation coefficient is calculated to be $1.42 \times 10^{-6}\ m/s$.

Simulations were conducted in a module containing the newly developed membrane in the FO mode for the solution volume flow rate of 1 $L\, min^{-1}$ in the feed and draw channel. The inlet mass fraction concentration of the draw solution was set to 0.05844 which corresponds to 1 M NaCl. The concentration difference across the membrane yields an osmotic pressure of 4.7 MPa that is determined using the empirical relation described in Eq 11. The membrane structural and physical parameters, the inlet concentration of the feed and draw solution, and the flow rate of solutions were matched between the validation study and experiments. The schematic and the dimensions of the validation test geometry are shown in Fig. 14. The inlet velocity of the feed and draw solution were set to 3.33 $m\, s^{-1}$ so that the volume flow rate is matched with the experiment. Net-type spacers were used in the feed and draw channel. The diameter of the spacers used was set to 0.5 mm and the angle between two spacer filaments was set to 90°. Reynolds number of the flow in both channels is calculated to be 5,533 based on the inlet velocity and the dimensions of each channel. The flow inside the feed and draw channel is turbulent and we utilize $k - \omega\ (SST)$ turbulent model for simulations. The averaged water flux is predicted to be 64.6 $L\, m^{-2}\, h^{-1}$ and the reported water flux at the same conditions is 70.3 $L\, m^{-2}\, h^{-1}$. The predicted flux deviates 8.10 % from the measured flux reported by Liang et al. [38]; validating the mathematical model and the numerical methods quantitatively.

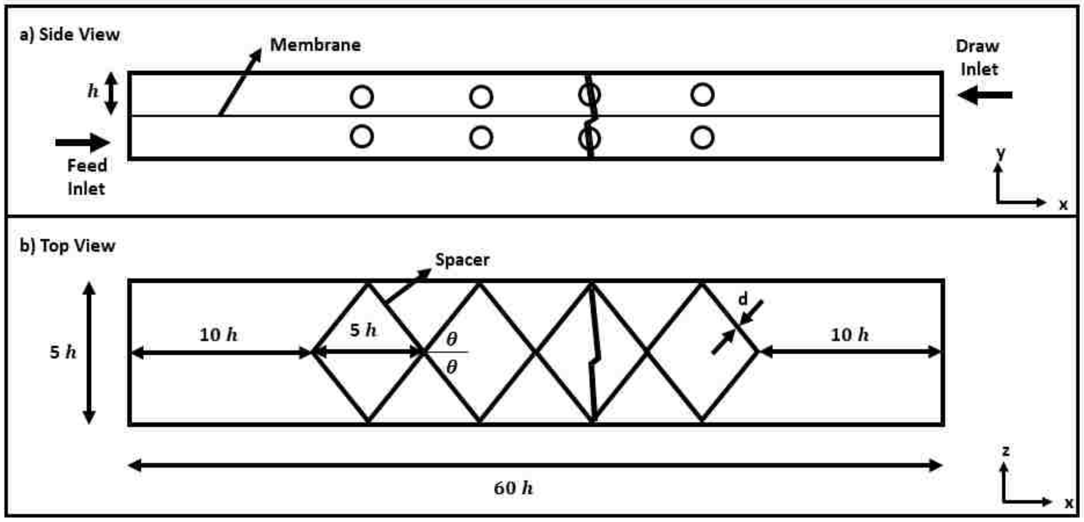

Figure 14. *Schematic for the geometry used in the validation*

In the rest of the simulations, the concentration of the feed solution was set to 0.004. This concentration of the feed side corresponds to a typical concentration of brackish water while the draw concentration is set to 0.09, a highly concentrated draw solution. It is usually difficult to separate pure water from highly concentrated draw solutions in the secondary stage of water desalination by forward osmosis [39]. However, this value is taken since it is the maximum concentration that can be used in the empirical relation in Eq. 11.

Results and Discussion

Contours of the normalized stream-wise velocity for Re = 300, 800 and 1500 are shown in Fig. 15 for four geometries – the channel corrugation, the single and double membrane corrugation and the combined channel and the membrane corrugation. The flow images are rendered in the middle section of the feed channel at $y/h = 0.5$ and $23.5 < x/h < 46.5$ for each geometry. Velocity contours are normalized with the average inlet velocity for each respective case. At Re = 300 the corrugation yields high-velocity regions in the major portion of the plane with velocity distribution following patterns of chevrons, as shown in Fig. 15 (a1, b1, c1, d1). The velocity magnitude over this plane is much higher in the geometry with the double and combined corrugations compared to the geometry with the single membrane corrugation and the channel corrugation only. The highest velocity is observed in the geometry with the combined corrugation at Re = 300. As Re is increased to 800 and 1500, the velocity pattern in the $y = 0.5h$ plane changes drastically. High-speed flow region shrinks to the center, and the visible chevron patterns disappear. We still see the spatially repeated flow patterns with the wavelength that is nearly the same as the length of the spacing between the successive chevrons. The high-velocity regions coincide with the regions near the intersection of the ribs. In all geometries, the high flow speed regions are seen in the middle, and lower flow speed regions are observed near the periodic surfaces at $z/h = 0$ and 5. These flow patterns indicate the presence of strong secondary flows inside the feed channel induced by the chevrons. The vortical activities induced by the secondary flows are favorable since they produce mixing in the feed channel. The enhanced mixing helps in reducing the external concentration polarization, and thus improves membrane performance.

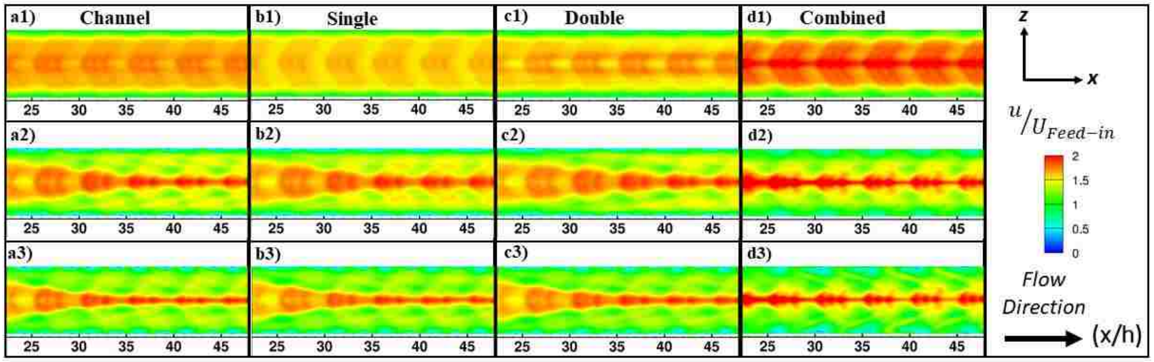

Figure 15. Contours of the stream-wise velocity in the feed channel for all cases. The normalized contours are taken at Re = 300 (a1, b1, c1, d1), Re = 800 (a2, b2, c2, d2) and Re = 1500 (a3, b3, c3, d3).

Fig. 16 illustrates the normalized stream-wise velocity contours in the draw channel for Re = 300, 800 and 1500. The velocity contours are normalized with the average inlet velocity for each geometry. The contours were rendered in the middle of the draw channel at y/*h* = 1.5. In the feed channel, the solution strikes the sharp tip of the ribs' intersection. While in the draw channel the solution strikes the left and right ribs and converges to the ribs' intersection. Thus, the flow fields in each channel are strikingly different except for the geometry with channel corrugation. The wall corrugation produces a similar flow field in both channels since the corrugation was oriented towards the flow direction in each channel. The single type of membrane corrugation has negligible effects on the velocity field in the draw channel. The reason is that the flow in the draw channel is not obstructed by the membrane corrugation since they are oriented to the feed channel. The membrane in the draw side has only dips which hardly alter the velocity field at any flow rate. In the double corrugated membrane and the combined geometry, the higher velocity regions tend to be near the periodic surfaces at z/*h* = 0 and 5. The middle of the channel experiences low speed flows. As the flow rate is increased, the intensity of the secondary flows induced by chevrons in the draw channel is increased. With the increased level of mixing intensity, the water permeation rate is expected to be increased, and the dilutive external concentration polarization is expected to be reduced.

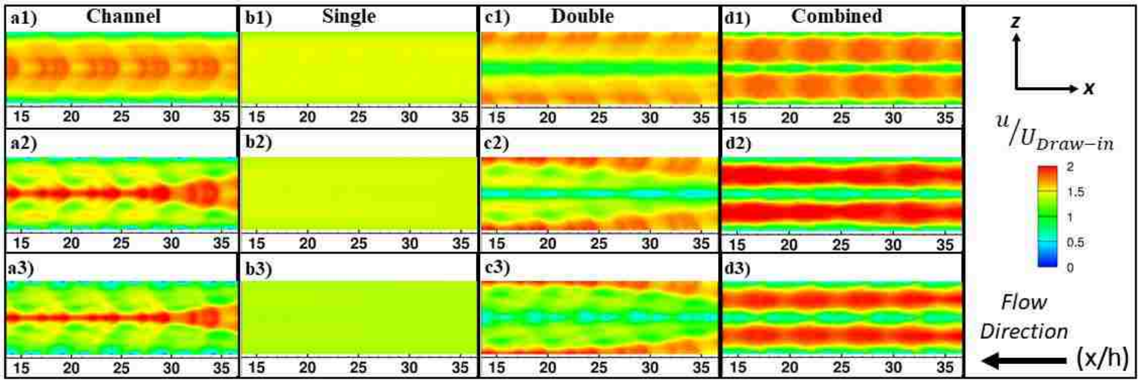

Figure 16. Contours of the stream-wise velocity in the draw channel for all cases. The normalized contours are taken at Re = 300 (a1, b1, c1, d1), Re = 800 (a2, b2, c2, d2) and Re = 1500 (a3, b3, c3, d3).

The contours of the normalized concentration along the membrane surface in the feed channel for Re = 300, 800, 1500 are shown in Fig. 17. The concentration contours are normalized with the inlet feed concentration. Ideally, in the feed channel, the normalized concentration of the feed solution should be near unity. However, the inevitable phenomenon called the external concentrative CP prevents that from happening. Enhanced mixing in the feed channel is expected to help in alleviating this problem. At Re = 300, in the geometry with the channel corrugation, the salt concentration is higher in the middle region of the membrane while it is lower in regions near the periodic surfaces. In the geometry with the single corrugation membrane, the high concentration polarization region is not observed. The region where ribs intersect has low concentration levels which are favorable in the feed channel. By comparing with contours of flow images and surface concentration (see Fig. 15(b1) and Fig. 17(b1)) it is noticed that high-velocity regions correlate well with the lower concentration regions along the membrane surface. In geometries with the double corrugation membrane and the combined corrugation, high salt concentration is observed in regions near the dip of chevrons and the low concentration is observed near the intersection of the ribs. The presence of the channel corrugation did not help in alleviating the high concentration spots inside the dips in the feed channel. As Re is increased to 800, the concentration level is decreased in the corrugated channel; only distinct wavy lines of high concentration regions are observed. Also, the lower levels of concentration are observed near the periodic surfaces. In the single corrugation, the region of low feed concentration has expanded compared to that for Re = 300. The concentration polarization in the feed channel in the double and combined corrugation geometries is reduced with the increase of flow rates, but the high concentration spots are still present inside the dips. At Re = 1500, the high concentration regions have reduced significantly in all four geometries. It has been shown in several studies that the higher flow rate corresponds with the lower concentration polarization [12,16,17]. A large portion of the membrane surface approaches the optimum value of the concentration polarization of unity as the flow rate is increased. Table 4 shows the averaged values of concentration polarization over the membrane surface in the feed channel. The modules with the combined corrugation and double corrugation have higher averaged concentration polarization at all flow rates while the single corrugation module has the lowest concentration polarization, as listed in Table 4. Images rendered in Fig 17 appeared to be conflicting with this conclusion by signifying the very low level of concentration over the membrane surface in the combined and the double corrugation geometry. To better characterize the membrane polarization characteristics, we examine the concentration profiles in these modules.

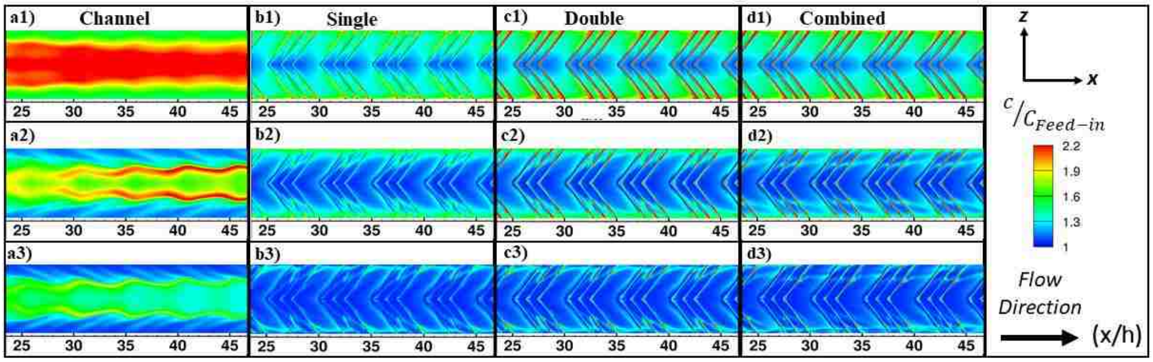

Figure 17. Contours of the concentration along membrane surface in the feed channel for all cases. The normalized contours are taken at Re = 300 (a1, b1, c1, d1), Re = 800 (a2, b2, c2, d2) and Re = 1500 (a3, b3, c3, d3).

Table 4. Averaged external concentrative concentration polarization

Re	Case				
	Empty	Channel	Single	Double	Combined
300	2.19	1.94	1.42	2.03	2.18
800	1.77	1.54	1.26	1.44	1.44
1500	1.59	1.33	1.16	1.22	1.23

Figures 18 and 19 depict the profiles of the normalized concentration over the membrane surface at $z/h = 2.5$ and $z/h = 0$, respectively, for Re = 300. The concentration profiles in corrugated geometries are compared to the profiles acquired in the module without corrugation. In the combined and the double corrugation geometry, the concentration level in a major portion of the membrane surface is as low as that in the single corrugation geometry, but there are spikes of concentration observed in the dips, as seen in Figs. 18 and 19. These spikes raise the average concentration over the membrane surface in the combined and the double corrugation geometry. The most significant finding from these profiles in corrugated modules is that the repeated patterns of concentration distribution in the streamwise direction; indicating that the level of concentration polarization is independent of the length of the module. In modules containing corrugations, the average concentration in the corrugated section is nearly constant, while the average concentration increases as the length increases in the module without corrugations. Such observation is especially true for the membrane corrugation cases, but not clear for the channel corrugation geometry. In the module with channel corrugation, the concentration increases with the length at z = 2.5*h* but reaches nearly an asymptotic value in the corrugation section at z = 0, as shown in Figs 18 and 19. The polarization remedies achieved by corrugation will be amplified in longer FO modules typically used in commercial applications. Our results also clearly demonstrate that further optimization study in these modules should be conducted to further improve performance by tuning the design of corrugations.

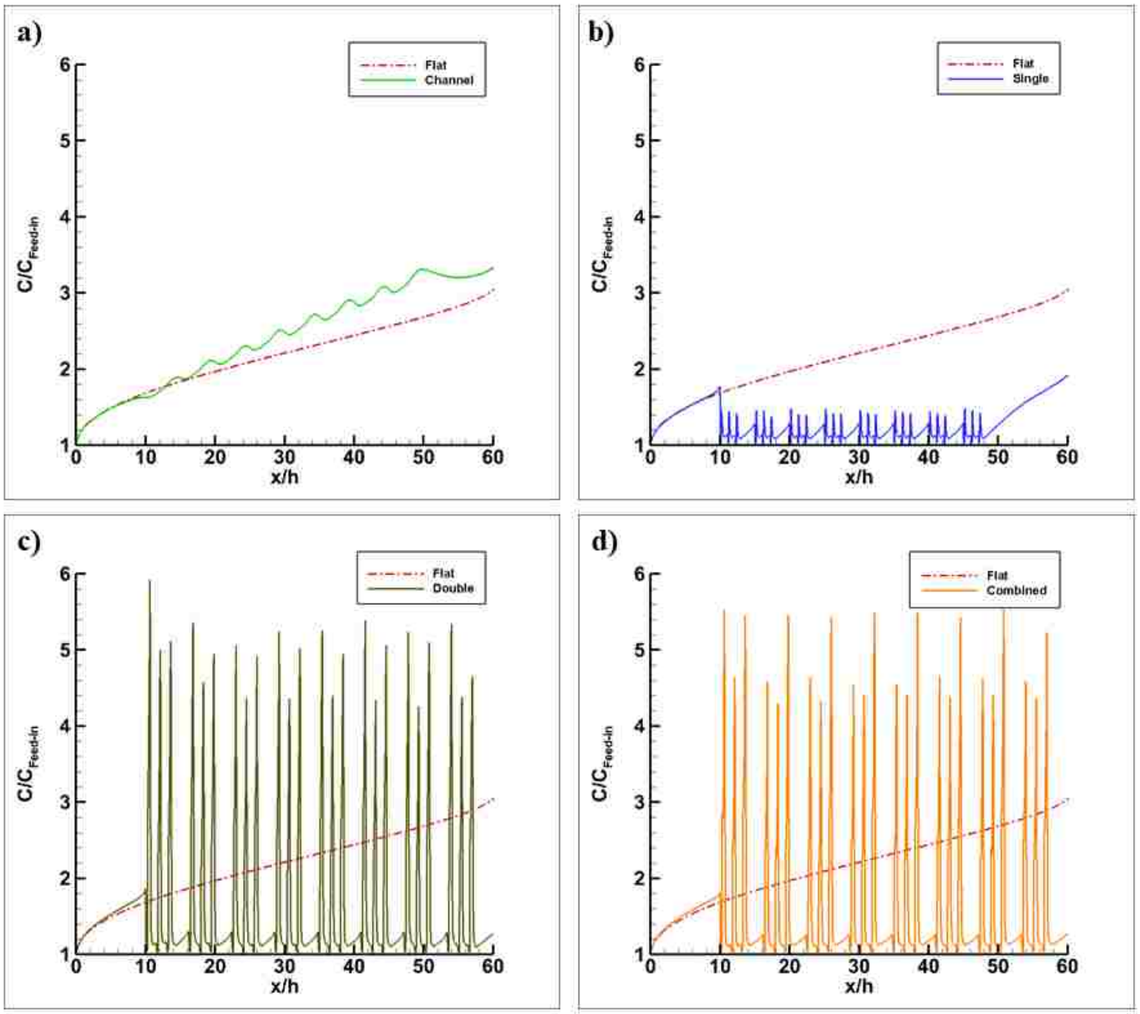

Figure 18. Profiles of concentration along the membrane surface at the feed side in all geometries at z/h = 2.5. (a) The channel corrugation and no corrugation, (b) the single membrane corrugation and no corrugation, (c) the double membrane corrugation and no corrugation, and (d) the combined corrugation and no corrugation.

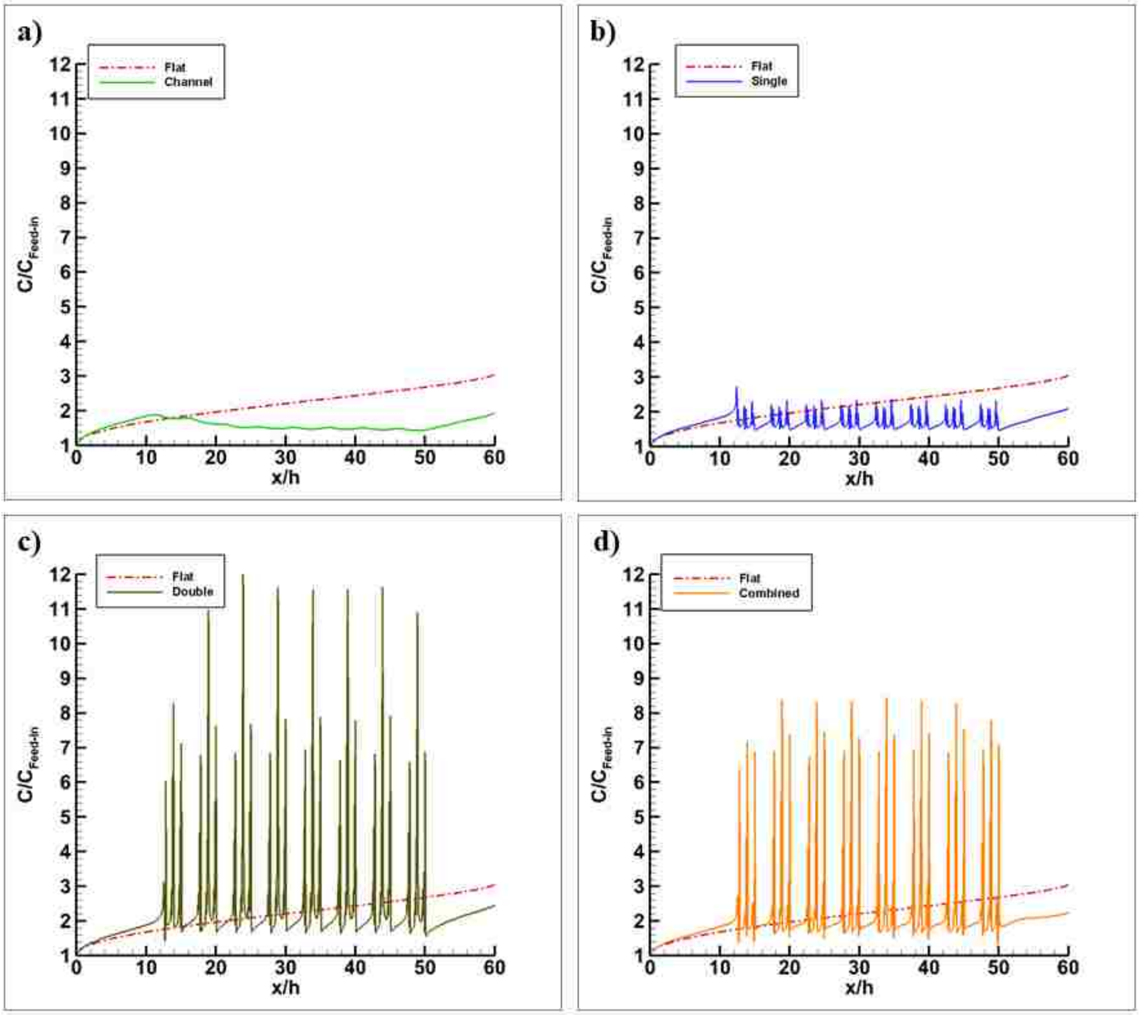

Figure 19. Profiles of concentration along the membrane surface at the feed side in all geometries at z/h = 0. (a) The channel corrugation and no corrugation, (b) the single membrane corrugation and no corrugation, (c) the double membrane corrugation and no corrugation, and (d) the combined corrugation and no corrugation.

Fig. 20 shows the normalized concentration along the membrane surface in the draw channel at Re = 300, 800 and 1500. The contours are normalized with the inlet draw concentration. In an ideal scenario, the concentration distribution along the membrane surface in the draw channel should be equal to the inlet draw concentration. However, since there is water permeation through the membrane surface the value of the bulk draw concentration drops. This phenomenon is called external dilutive concentration polarization. For better membrane performance the flow in the draw channel should be mixed so that the bulk concentration in the channel can be brought near the membrane surface. From Fig. 20 (a1, b1, c1, d1) the contours of the draw membrane in the channel case shows a drop in the concentration levels along the membrane surface similar to the trend seen in Fig. 18(a1) in the feed channel. In the single corrugation, lower values of concentration are seen in middle of the membrane near the ribs intersection. Also, a high region of concentration happens near the periodic surfaces. The double and combined corrugation cases follow a similar trend. Spots of low-level concentration are observed inside the dips in both cases. In Fig. 20 (a2, b2, c2, d2), the concentration contours in the channel corrugation case shows a higher concentration near the periodic surfaces. The single corrugation case shows better mixing than Re = 300 and the best mixing happens on the edges at z/h = 0 and 5. Since this region corresponds to the corner were two ribs meet in the flow direction. For the double and combined corrugation cases, a highe level of concentration is seen. Again, the lower concentration is seen in the middle of the membrane because of the low mixing that happens in this region. For Re = 1500 (a3, b3, c3, d3), the concentration level increases in all cases. The spots of low concentration inside the membrane dips have disappeared. Table 5 shows the averaged values of concentration polarization over the membrane surface in the draw channel. The double corrugation case shows the highest concentration polarization, but the combined case also has similar polarization level as for the double case. At the same time, the single corrugation yields the lowest level of concentration polarization.

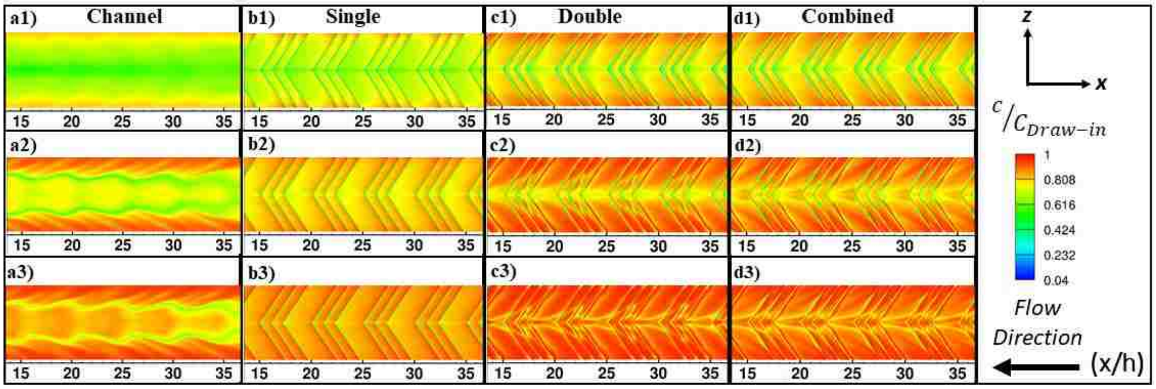

Figure 20. Contours of the concentration along membrane surface in the draw channel for all cases. The normalized contours are taken at Re = 300 (a1, b1, c1, d1), Re = 800 (a2, b2, c2, d2) and Re = 1500 (a3, b3, c3, d3).

Table 5. Averaged external dilutive concentration polarization

Re	**Case**				
	Empty	**Channel**	**Single**	**Double**	**Combined**
300	0.65	0.69	0.66	0.75	0.75
800	0.71	0.78	0.75	0.83	0.82
1500	0.74	0.83	0.80	0.88	0.87

Fig. 21 shows the normalized shear stress along the membrane surface in the feed side for Re = 300, 800 and 1500. The shear stress is normalized based on the maximum shear stress that occurs in the region between 23.5 < x/*h* < 46.5 for each geometry. The magnitude of the membrane wall shear stress could be used as another measure of the membrane performance. High-shear regions correlate strongly to low-fouling regions over the membrane surface [15]. Fouling is the buildup of salt and particulate over the membrane surface. The more buildup there is less water permeation over the membrane surface. For Re = 300, the channel corrugation contours show higher wall shear stress regions over the membrane surface. The high wall shear stress is attributed to the fact that the corrugation lies in the bottom of the feed channel and the feed solution will be directed toward the membrane surface causing the high wall shear stress. In the other three geometries, a similar trend is seen for the wall shear stress. The higher-level shear stress is observed near the ribs' intersection while the lower-level of shear stress occurs behind the ribs. This is more pronounced in the double and combined geometries since there are dips along the membrane surface in both cases. At Re = 800, the higher shear stress regions over the feed membrane in the channel corrugation become smaller. A similar trend is seen for the other three geometries. The higher shear stress is observed behind each group of ribs in the single geometry compared with the double and the combined geometries. The distribution of the wall shear stress has repeated patterns since the flow is hydrodynamically developed in the section of the channel where contours are rendered. The repeated patterns of the shear stress over the feed membrane for Re = 1500 are very similar to those observed for Re = 800. The only difference is that the high shear stress regions between the ribs grow toward the periodic surfaces, as depicted in Fig 21. Table 6 shows the maximum shear stress values over the membrane surface in all geometries for Re = 300, 800 and 1000. The magnitude of membrane wall shear stress is greater immensely in modules with corrugations compared to that in a module without the corrugation at all Re, especially at higher flow rates. The magnitude of the shear stress is increased as the flow rate is increased in all geometries. It is noticed that the wall shear stress is higher in geometries with corrugated membrane compared to that in the geometry with corrugated channel wall. The wall shear stress level is the highest in the geometries of the double and the combined corrugation. The corrugated modules outperform the modules without corrugation since fouling will be less likely with corrugation.

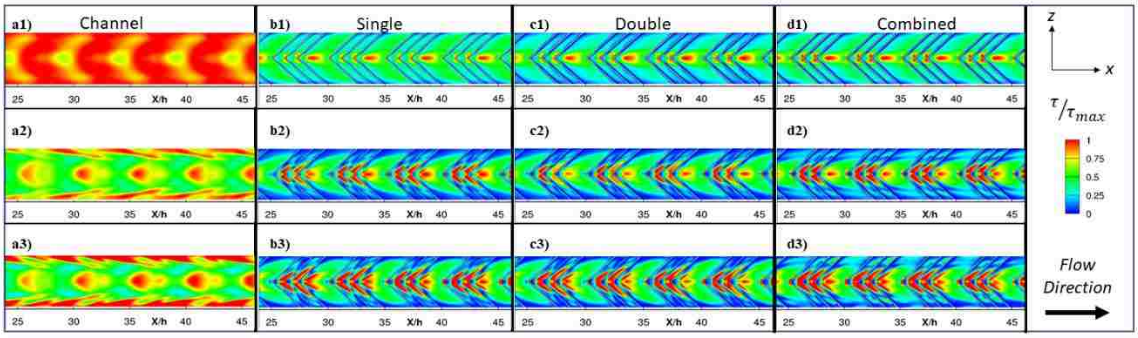

Figure 21. Contours of the shear stress along membrane surface in the feed channel for all cases. The normalized contours are taken at Re = 300 (a1, b1, c1, d1), Re = 800 (a2, b2, c2, d2) and Re = 1500 (a3, b3, c3, d3).

Table 6. *Maximum shear stress values over the membrane surface in feed channel – all values are in the unit of Pa*

Re	**Case**				
	Flat	**Channel**	**Single**	**Double**	**Combined**
300	1.09	1.32	2.24	3.0	2.7
800	3.04	6.40	15.2	16.0	20.0
1500	5.75	16.90	40.0	41.0	51.0

Fig. 22 shows the normalized water flux through the membrane. The water flux is normalized with the membrane pure water permeability and the difference in osmotic pressure between the feed and draw channels. The water flux is a major indicator in the performance of the membrane system as it is the required output from such systems. The water flux is calculated from Eq. 12; thus, the effect of the porous support layer is included in the contours shown in Fig. 22. However, changing the flow field inside the channel will not have any effect on the internal dilutive concentration polarization. Only external dilutive concentration polarization and external concentrative concentration polarization are affected by the flow field induced by the corrugation at the channel wall and/or at the membrane surface. Hence, altering flow field in the feed and draw channel has limited influence on the flux performance in FO modules compared to that in the RO modules [15,17,40]. In the geometry with the channel corrugation, there is a very low water permeation through the membrane surface over the middle of the membrane at Re = 300. The double and combined corrugation geometries show higher water flux compared to the single corrugation. Also, the regions in front of the ribs show a low level of water permeation. For Re = 800, the water flux in the channel geometry increases. The water flux patterns differ among the double, combined and the single corrugation geometries. The water permeation is significantly higher in the double and combined geometries for the higher flow rate. As the flow rate is increased further to Re = 1500, each geometry yields the higher water permeation. Table 7 shows that the highest water flux enhancement is for the combined geometry for Re = 300, and the lowest flux enhancement is attained in the geometry with the channel corrugation. Although the water permeation is an important factor to consider it is not the only factor that determines the performance of the membrane system. The concentration polarization and the fouling are immensely important performance measures in these separation systems as stated above.

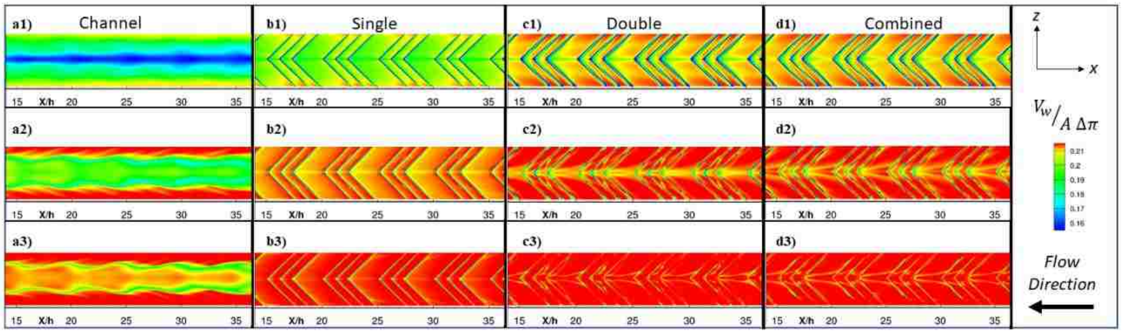

Figure 22. Contours of the water flux along membrane surface for all cases. The normalized contours are taken at Re = 300 (a1, b1, c1, d1), Re = 800 (a2, b2, c2, d2) and Re = 1500 (a3, b3, c3, d3).

Table 7. Averaged water flux and percentage enhancement for all cases

	Case														
	Empty			**Channel**			**Single**			**Double**			**Combined**		
Re	**300**	**800**	**1500**	**300**	**800**	**1500**	**300**	**800**	**1500**	**300**	**800**	**1500**	**300**	**800**	**1500**
Flux $[kg/m^2h$	56.37	62.21	65.27	60.75	67.96	72.13	63.97	69.52	72.73	64.23	71.12	74.75	64.70	71.32	74.60
Enhancement %	-	-	-	7.77	9.24	10.51	13.48	11.75	11.43	13.94	14.32	14.52	14.77	14.64	14.29

We have described above the spatial characteristics of the flow and concentration fields in various geometries consisting of the corrugated forward osmosis membranes and channel walls. To assess the membrane performance, a balance between the desired output and the required input to the FO module is needed. The pumping power is the required input for the improved flux realized with the application of corrugations. The coefficient of performance is introduced to compare each module with the base geometry without corrugation at the same flow rate. The coefficient of performance *COP* is given by

$$COP = \left(\frac{J_{wc}}{J_{we}}\right)\left(\frac{\left(f_f+f_d\right)_e}{\left(f_f+f_d\right)_c}\right)^{1/3} \tag{25}$$

where J_w is the averaged water flux of module,f_f and f_d are the averaged friction factor for the feed and draw channels, respectively. The subscript *c* denotes properties of modules including corrugated membrane and the channel wall and the subscript *e* denotes properties of modules consisting of the flat membrane and the flat channel walls. The friction factor for the draw or the feed channel is calculated as

$$f = \frac{2\,h\,\left|\frac{dp}{dx}\right|}{0.5\,\rho\,U_{ave}^2} \tag{26}$$

where $\left|\frac{dp}{dx}\right|$ is the pressure gradient in the stream-wise direction. Table 8 shows the average friction factor values along with the calculated *COP* for all cases. The modules with the single and double corrugation FO membranes have a *COP* slightly greater than unity at Re = 300. A *COP* of less than unity implies that there is no value added by the corrugation when the pumping power is considered. However, the concentration polarization is an important performance factor that is not included in the definition of *COP*. Tables 4 and 5 show a significant improvement in the external concentrative or the external dilutive concentration polarization within the corrugated modules. A mitigation of concentrative concentration polarization is an indicator of less potential fouling to be expected over the membrane surface and thus a better membrane performance over the long run.

Table 8. Average friction factor for both feed and draw channels and the coefficient of performance for all geometries

Re	**Case**													
	Flat		**Channel**			**Single**			**Double**			**Combined**		
	f_f	f_d	f_f	f_d	COP	f_f	f_d	COP	f_f	f_d	COP	f_f	f_d	COP
300	0.26	0.29	0.35	0.43	**0.96**	0.34	0.31	**1.07**	0.36	0.4	**1.03**	0.47	0.49	**0.95**
800	0.12	0.13	0.24	0.29	**0.84**	0.22	0.13	**0.98**	0.22	0.24	**0.93**	0.42	0.30	**0.80**
1500	0.07	0.08	0.20	0.26	**0.76**	0.19	0.09	**0.91**	0.19	0.20	**0.83**	0.40	0.25	**0.70**

Conclusion

This work focuses on studying the effects of the membrane and channel corrugation on the membrane performance in forward osmosis modules. Computational fluid dynamics simulations are conducted in three dimensional FO modules consisting of corrugations over the channel walls and membranes. The laminar flow model is utilized in the module with flat channel walls and membranes surfaces while the shear stress transport $k-\omega$ turbulence model is utilized in modules consisting of corrugated channel walls and/or the corrugated membranes of different arrangements for Reynolds numbers of 300, 800 and 1500. A modified version of the solution-diffusion model was used to calculate the water flux through the membrane by including the effect of the porous support layer. The flux model was validated against the existing experimental work with a good match between the prediction and the experimental results.

The flow and concentration fields in forward osmosis membrane modules containing corrugations are characterized. Performance of the modules with channel wall corrugation, the single and double membrane corrugations and the combined wall and membrane corrugations were determined and compared with the performance of the FO module without corrugations. Our results show that corrugation helped in mixing both feed and draw solutions except in the draw channel of the single corrugation geometry. Similarly, the corrugations helped in alleviating the external concentrative concentration polarization and the external dilutive concentration polarization except in the single corrugation geometry at the draw side. The corrugation also helped in increasing the shear stress over the membrane surface in both sides. The increase of the shear stress over the membrane surface could help in reducing the potential fouling over the membrane. Membrane corrugation produced higher shear stress than channel corrugation as expected. The highest water flux was obtained in the geometry with the double corrugation at Re = 1500, and the lowest flux was obtained in the geometry with the channel corrugation at Re = 300. The *COP* value of less than unity except the single and double corrugation geometries at Re = 300 was obtained. The combined geometry at Re = 1500 yielded the lowest value of *COP*.

Chapter 5: Characterizing embedded-spacer membranes in forward osmosis membrane modules

Computational fluid dynamics simulations are conducted on a forward osmosis desalination module. The effect of the porous support layer on forward osmosis membranes is neglected. However, the ECP is an inherent phenomenon that will be present in any FO or PRO systems with any membrane. Most research conducted in FO focused on alleviating the ICP by designing innovative membranes where little extensive investigation is focused on curing ECP. Several researchers indicate in their experimental work that spacers were placed within the feed, the draw or both channels to enhance mixing and support the membrane. While this is true, the existence of spacers might not completely mix the feed or the draw solutions. This lack of mixing might also lead to high fouling over the membrane surface in the feed channel. Also, the existence of spacers adds extra pressure drop within the feed and the draw channel which leads to more power consumption to operate such systems.

In this chapter, the novel membrane design is proposed and explored through computational fluid dynamics simulations (CFD). This innovative design consisting of a spacer embedded membrane aims to enhance mixing the feed and the draw channels with minimal pressure drop. This new design can also help in supporting the membrane. A net-type spacer will be embedded within the membrane structure. Three spacer diameters will be simulated. A flat membrane will be used a benchmark for comparing the performance of each spacer-embedded membrane. The laminar model will be used for the flat membrane while the k-ω SST model is used to model spacer-embedded membranes. The flow rate will be varied such that the Re is 300, 800, and 1500 in each case. Also, the effect of the porous support layer will be neglected since it was shown by Li et al. [31] that this is a plausible assumption.

The results indicate that the case with D = 0.3h have alleviated the dilutive and concentrative external concertation polarization substantially. Also, the case with D = 0.3h and Re = 300 performed better. The cases with D = 0.1h and Re = 300 and D = 0.3h and Re = 1500 had the worst overall performance.

Numerical Model, Convergence, and validation

A schematic diagram for the embedded spacer is shown in Fig. 23. From Fig. 23(a) shows the side view of the embedded spacer as it is inserted between two active layers of the membrane. Fig.23(b) shows the top view of the membrane. Eight cells of the spacer are considered in the simulations. The height of each channel is h, the width of the channels is 5h, and the length of the module is 60h. The angle between the horizontal and each strand of the spacer is $\theta = 45°$. The diameter of the spacer strand is denoted as D in Fig.23 (a). There are three geometries developed in this work that have the same dimension as shown in Fig. 23 (a) except the spacer's diameter. Three different spacer's diameters were considered as D1 = 0.1h, D2 = 0.2h, and D3 = 0.3h. Each spacer diameter was simulated with three different flow rates that correspond to different Re as 300, 800, and 1500.

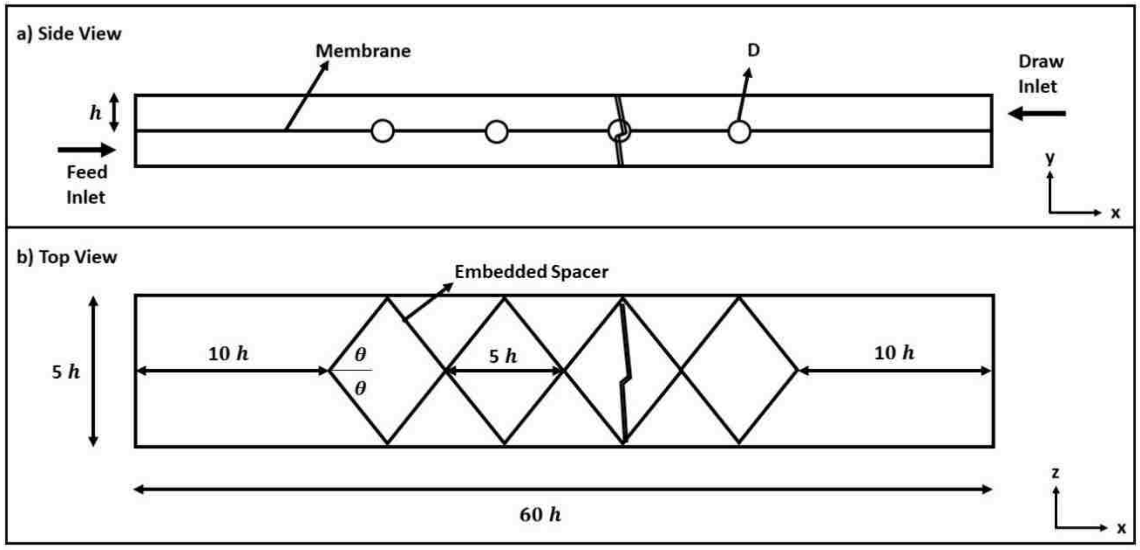

Figure 23. Schematic diagram for the geometry (a) side view showing both channels (b) a top view that shows the spacers arrangement.

The pure water permeability of the membrane used in the current simulations was taken from the membrane developed by Liang et al. [38], and it is estimated to be $4.71 \pm 0.22\ L\ m^{-2}h^{-1}bar^{-1}$. In their work, they have reduced the effect of the porous support layer drastically by tailoring the orientation of the porous pores in a cylindrical manner. However, the effect of the dilutive internal concentration polarization is still present. Therefore, based on the stated literature review, the effect of the porous layer was completely eliminated while keeping the same properties fixed. The osmotic transmembrane pressure $\Delta\pi$ was set to $2\ MPa$ by using a brackish water of 0.004 solute mass fraction (4000 ppm) and a draw solution of solute mass fraction equivalent to 0.0288 (28,800 ppm).

The computational domain was meshed using Ansys meshing tool. The mesh was unstructured with tetrahedral elements. An inflation near the membrane was used to capture the external concentration polarization that happens in both channels. The first layer thickness of the inflation layers was $5\ \mu m$ [9]. The number of mesh used in all the simulations listed in the above table were 20 million elements. The number of mesh was determined using a mesh optimization test. The case with D = 0.3*h* and Re = 1500 was used in the optimization test. Three mesh densities M1, M2, and M3 were utilized corresponding to a total number of mesh as 10 million, 20 million, and 40 million, respectively. Fig. 24 shows a summary of the mesh optimization results were the local variation of the feed and the draw concentrations were compared with the three different meshes. Also, the stream-wise velocity in the middle of the feed channel were monitored. Fig. 24 (a) shows the concentration polarization over the membrane in the feed channel at z/*h* = 2.5. The variation of concentration matches with all the three meshes everywhere except at the peaks of the variation were slight deviation is observed. Fig. 24 (b) shows the variation of the normalized stream-wise velocity in the feed channel at y/*h* = 0.5 and z /*h* = 2.5. Perfect match is observed near the inlet of the module. Some deviation is observed near the exit. Furthermore, the velocity signature shows that the flow is fully developed at the last third of the module. Fig. 24 (c) shows the concentration polarization over the membrane in the draw channel at z/*h* = 2.5. the variation of the concentration is identical in the three meshes, the bottom of the variation shows slight deviation with M2 and M3. Fig. 24 (d) shows the vertical variation of the feed concentration from the bottom of the feed channel to the top at z/*h* = 2.5. Perfect match is seen in all the three different meshes. Based on the results presented in Fig. 24, a mesh of 20 million elements were chosen to conduct the rest of the simulations in this work. A section of the used mesh is shown in Fig. 25.

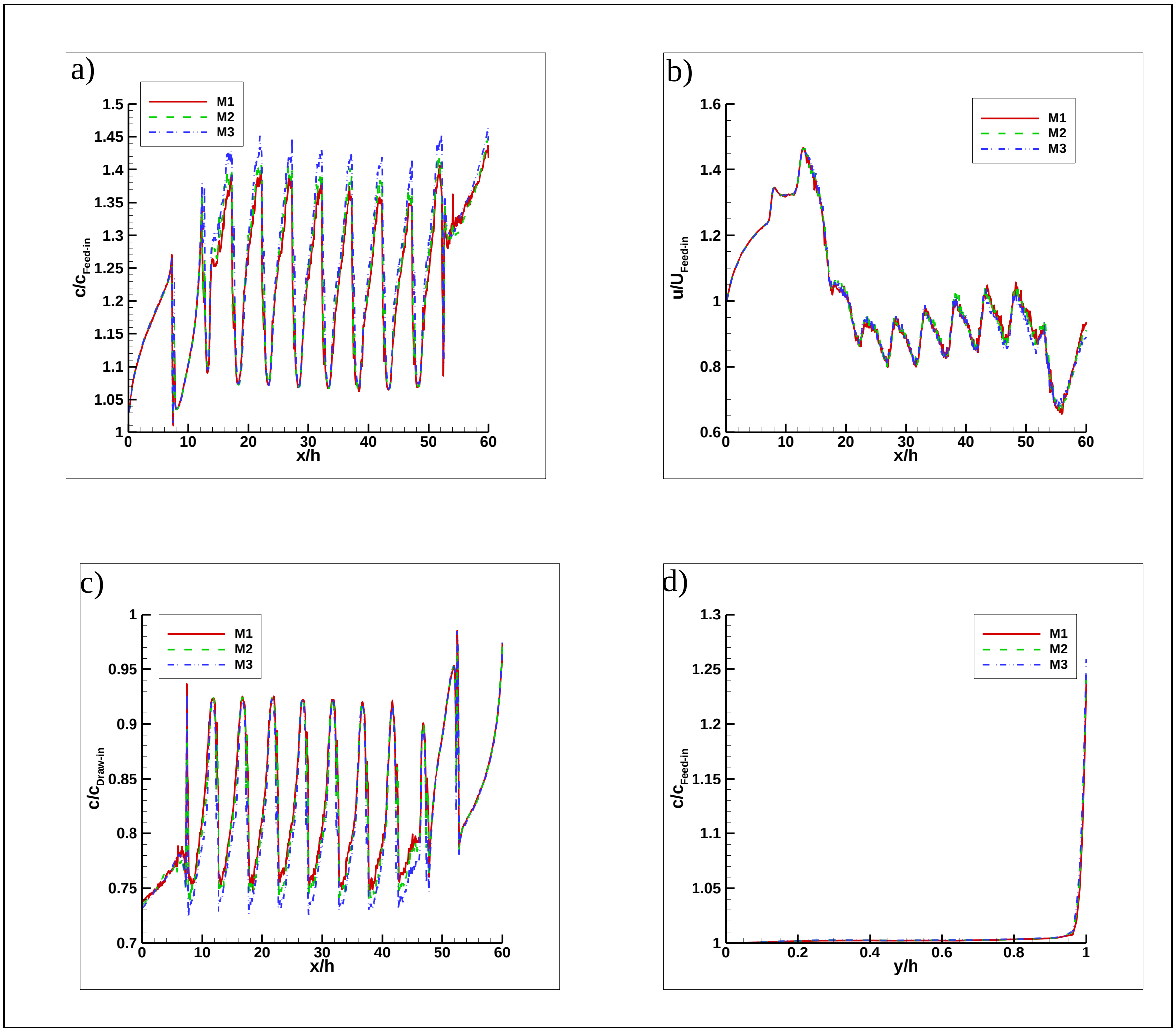

Figure 24. Profiles of (a) the normalized concentration along the membrane in the feed channel at z/h = 12.5 from the inlet to the outlet, (b) The normalized stream-wise velocity in the feed channel at y/h = 0.5 and z/h = 25 from the inlet to the outlet. (c) The normalized concentration along the membrane in the draw channel at z/h = 12.5 from the inlet to the outlet. (d) The normalized concentration along the height in the feed channel at x/h = 25 and z/h = 2.5 from the bottom of the feed to the top. Profiles obtained using the mesh density of 1, M2, and M3.

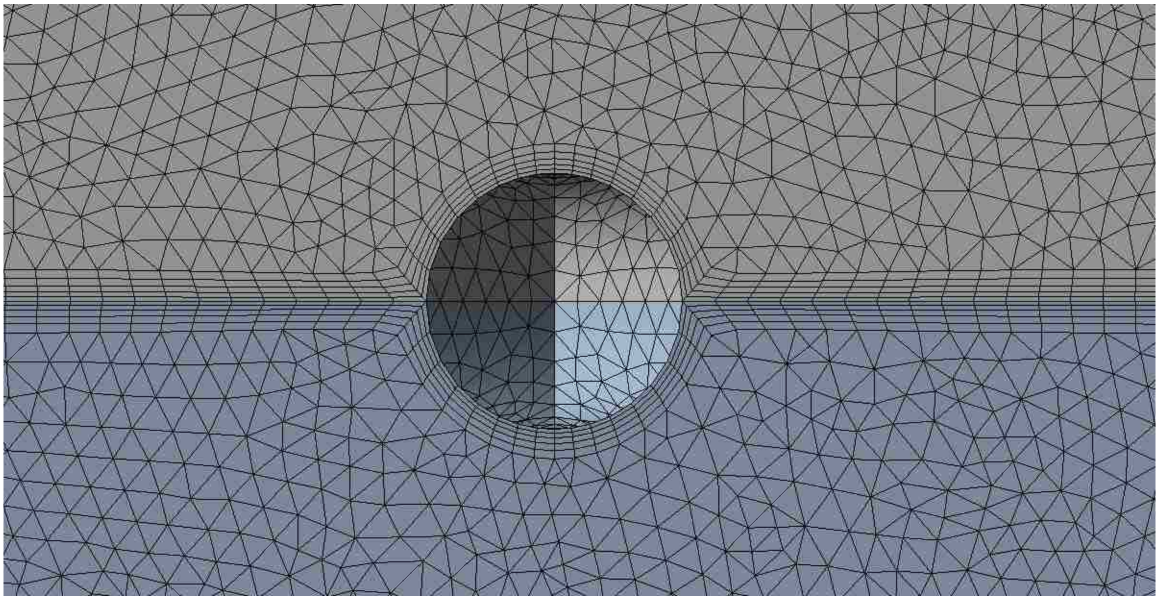

Figure 25. *Section of the mesh used that shows the inflation layer near the membrane with the embedded spacer*

Results

A validation study is performed in the modeled used in the experimental study by Li et al. [31]. In their experiments, they used the newly developed membrane which is a support-free membrane in which the porous support layer was eliminated. Only an active layer is present. The pure water permeability coefficient for the membrane with a thickness of $5\ \mu m$ was estimated to be $0.16\ \mathrm{L\ m^{-2}\ h^{-1}\ bar^{-1}}$. The test was conducted in a cell with known dimensions of $78\ \times 25\ \times 5\ mm$. The feed and the draw solutions used were comprised of a deionized water and Na_2SO_4 with different concentrations, respectively. The velocity of the solutions in the test cell was set to $10.36\ cm/s$ which corresponds to Re of 860. The flow in the module without spacers is laminar. The same Reynold number was used in the CFD simulations to match the flow field of the experiment. Also, the draw concentration was varied from 0.4 to1.5 $mol\ L^{-1}$ of Na_2SO_4 with deionized water in the feed channel. The concentration of the draw solution in the CFD simulation was taken as $0.5\ mol\ L^{-1}$ since the relations given in the mathematical model for the physical properties of Na_2SO_4 are valid only for a mass fraction of less than or equal to 0.09.

The simulation results show that the water flux equals to $4\ kg/m^2h$. The reported water flux in the experiment given by Li et al. [31] under the same conditions is $4.35\ kg/m^2h$. The reverse solute flux from the simulation results is $2.88\ g/m^2h$. While the reported reverse solute flux is $3\,g/m^2h$. The deviation seen in the simulation compared with the experiment in the water flux and the reverse solute flux are 9% and 4%, respectively. Our CFD model is therefore considered to be validated.

It should be noted that both flux equations were used, i.e., eq. 10 and 12 in the validation study and the water flux predicted is similar. We employed eq. 10 in determining the water flux through the membrane since the effect of the porous layer is neglected.

Contours of the normalized stream-wise velocity for Re = 300, 800 and 1500 are shown in Fig. 4. The velocity contours normalized with the average inlet velocity are rendered in the middle of the feed channel at $y/h = 0.5$ and $22.5 < x/h < 47.5$. For $D = 0.1h$, it is observed that nearly all the contours follow a similar trend. The stream-wise velocity contours resemble a velocity contour for an empty channel. Faded high velocity regions are observed in the flow channel that takes the shape of the embedded spacer. This trend is observed for all Reynold numbers used. The flow is considered hydrodynamically developed since there is a clear, repeated structure in the contours. The stream-wise velocity in the middle of the draw channel for the same Reynold numbers have the same trend for the feed channel since the embedded spacers orientation is the same on both sides of the membrane.

The velocity behavior for D = 0.2*h* and Re = 300 is similar to that of D = 0.1*h* at the same Reynolds number. The only difference is that the spacers signature is more obvious in D = 0.2*h*. For Re = 800, the velocity contour starts to take a different behavior. There is a distinct horizontal low velocity region that cuts in the middle of the channel. The intensity of this low velocity region in the middle is heighten in Re = 1500. Also, the same low velocity region can be seen at z/h = 0 and 5 which is a region of strands intersection. Similar discussion can be given to the velocity contours in the draw channel for D = 0.2*h* as the feed channel since the Re and spacer geometry are identical.

The velocity contours at D = 0.3*h* and Re = 300 have similar characteristics as those for D = 0.1*h* and 0.2*h*. They share a similar feature with a distinct imprint of the spacers on the contours which corresponds to high velocity regions. For Re = 800, the results are different than the previous cases. The contour has divided to two distinct regions in each set of spacers. There is a distinct low velocity region that crosses the strands intersection which separates the high velocity region into two regions. Inside the high velocity region, there is still the imprint of the spacers which make an even higher velocity region. For Re = 1500, the same trend is observed as Re = 800. However, the high velocity region became the imprint of the spacers where the region away from the strand’s intersection became an intermediate velocity region. Since the flow rate and the geometry are the same in the draw channel, the same velocity contours are seen in the middle of the draw channel. The highest level of mixing in both the feed and draw channels is observed to be at Re = 800.

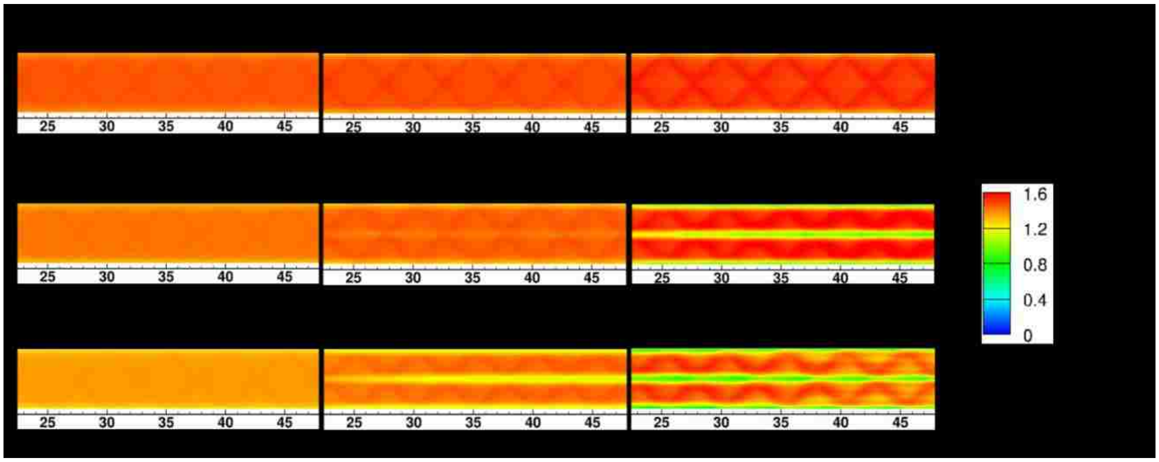

Figure 26. *Normalized stream-wise velocity in the middle of the feed channel for Re = 300 (a1, b1, c1), Re = 800 (a2, b2, c2), Re = 1500 (a3, b3, c3).*

Fig. 27 shows the normalized concentration contours along the membrane surface in the feed channel for Re = 300, 800, 1500. The contours are normalized with the inlet feed concentration. Since the embedded spacers are modeled as impermeable surfaces, there are white regions in the contours over the membrane surface. These regions are excluded from the results and the discussions, and they are only seen as the location for the embedded spacers. It can be seen from Fig. 27 (a1) that there is a high concentrative CP on the membrane surface. The region in the membrane between each successive intersection of the strands shows a distinct high concentrative CP region. The lower level of concentration is observed as the flow is far from the intersection region on both sides. For Re = 800 in Fig. 27 (a2), the bulk concentration is lower than Re = 300. Still, the intersection of the strands shows a high concentration region. Fig. 27 (a3) shows the concentration contours for Re = 1500. The concentration polarization is less compared to the previous cases. Similarity is also seen at the intersection of the ribs.

Fig. 27 (b1, b2, b3) shows the concentration contours over the membrane surface in the feed channel for D = 0.2h and Re = 300, 800 and 1500, respectively. The increase in spacers strand diameter shows an improvement to the level of concentrative concentration polarization over the membrane surface. The extreme high concentration levels seen in D = 0.1h for Re = 300 have been lowered with increasing the strand diameter by only 0.1h as seen in Fig. 5(b1). For Re = 800 and 1500, the concentration shows similar trends as before.

The case where D = 0.3h is performing much better regarding mitigating the concentration polarization over the membrane surface. For Re = 300, the middle line crossing the region where strands intersect shows a high concentration region. This line is dividing the membrane surface to two low concentration regions away from the center. For Re = 800, a similar trend is observed. However, the line that divides the membrane is thinner, and it is almost disappearing. As for Re = 1500, this line is the same compared with Re = 800. However, the concentration polarization is lower in the two regions next to the dividing line. Table 9 shows a summary of the average concentration polarization over the feed membrane in the feed channel for all flow rates considered.

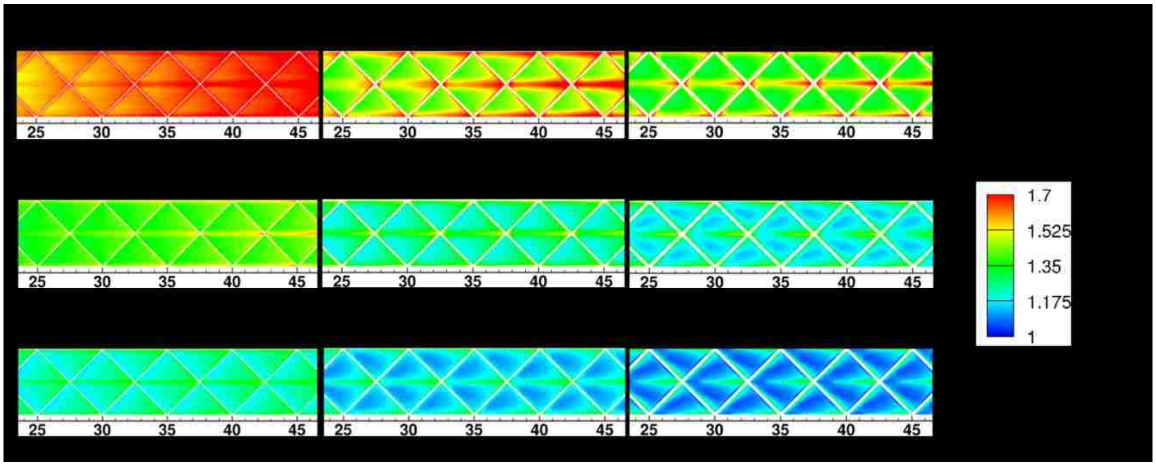

Figure 27. *Normalized contours of the external concentrative CP for Re = 300 (a1, b1, c1), Re = 800 (a2, b2, c2), Re = 1500 (a3, b3, c3).*

Table 9. Average concentrative external concentration polarization over the feed membrane in the feed channel

Re	Case			
	Flat	D = 0.1*h*	D = 0.2*h*	D = 0.3*h*
300	1.7	1.61	1.48	1.41
800	1.51	1.38	1.27	1.23
1500	1.41	1.23	1.18	1.15

Fig. 28 presents the local variation of the concentration in the feed channel over the membrane surface at z/h = 1.25. In Fig. 28 (a, b, c), the concentration is depicted from the inlet to the outlet of the feed channel. The feed concentration starts to increase as it enters the feed channel since there is mass transfer to the draw channel. As the feed solution touches the embedded-spacers, the feed solution is mixed with the bulk of the flow. This mixing behavior suppresses the increase of the feed concentration. Fig. 28 (a) shows the embedded spacer of D = 0.1*h*, the feed concentration in the flat membrane case continues to increase. The presence of the embedded-spacers suppresses the increase seen in the flat membrane case. Similar behavior is seen in Fig. 28 (b) and (c). However, the level of suppression is increasing as the embedded-spacers diameter increases. More mixing is observed with D = 0.3*h* as shown in Fig. 28 (c).

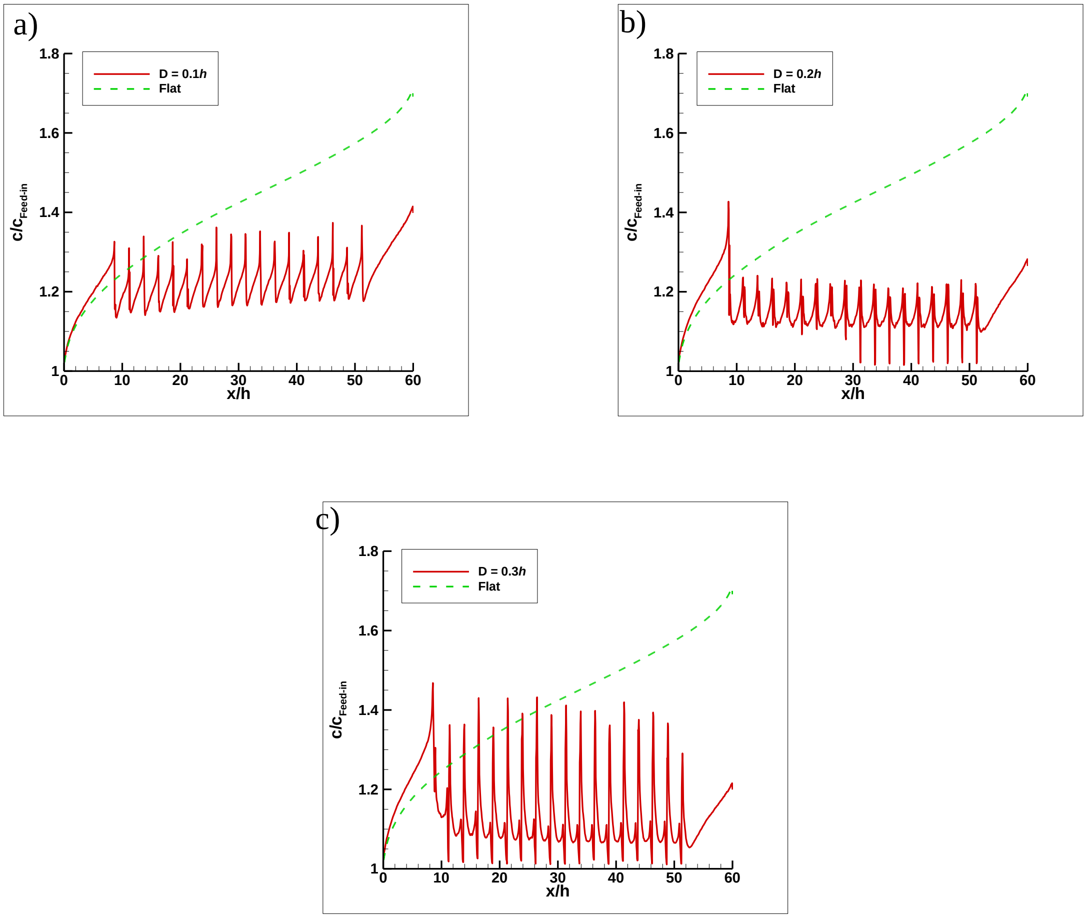

Figure 28. *Local variation of the feed concentration at z/h = 2.5 to compare the flat membrane case at Re = 1500 with (a) D = 0.1h (b) D = 0.2h (c) D = 0.3h*

Fig. 29 (a, b, c) shows the contours of the normalized external dilutive CP in the draw channel for Re = 300, 800 and 1500, respectively. Since the flow in the draw channel is similar to the flow in the feed channel, the concentration contours are also similar to the contours in the feed channel. The only distinct difference is that having a higher concentration over the membrane surface in the draw side is favorable. Also, there is no risk of fouling on the membrane surface in the draw side. The average dilutive CP for the cases of Re = 300, 800 and 1500 are 0.69, 0.76 and 0.82, respectively. Therefore, increasing the flow rate in the draw channel increases the dilutive CP and it is approaching unity.

For D = 0.2*h* and Re = 300, the low concentration regions tend to be in the spacer's cells and away from the center. For Re = 800, the distribution of the concentration is almost constant and fade regions of low concentration are observed in the middle of the spacer's cells. For Re = 1500, the high concentration regions are clearer, and they tend to be inside the spacer's cell and behind the spacer strand in the direction of the flow. A similar trend is seen in D = 0.3*h* as 0.2*h.* Table 10 shows the average dilutive concentration polarization for the membrane in the draw channel.

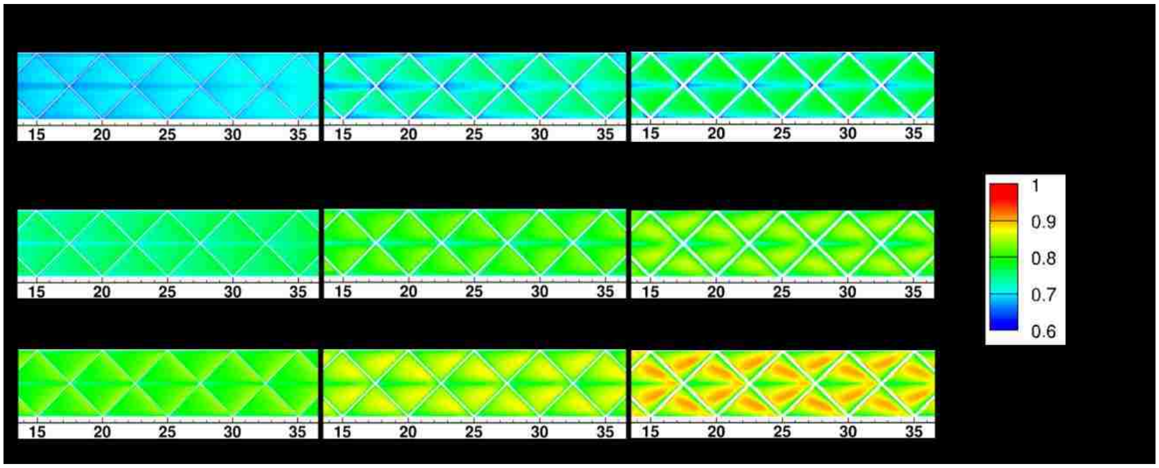

Figure 29. *Normalized contours of the external dilutive CP for Re = 300 (a1, b1, c1), Re = 800 (a2, b2, c2), Re = 1500 (a3, b3, c3).*

Table 10. Average dilutive external concentration polarization over the draw membrane in the draw channel

Re	**Case**			
	Flat	**D = 0.1*h***	**D = 0.2*h***	**D = 0.3*h***
300	**0.67**	**0.69**	**0.73**	**0.75**
800	**0.71**	**0.76**	**0.80**	**0.82**
1500	**0.74**	**0.82**	**0.85**	**0.87**

Fig. 30 (a, b, c) shows the normalized wall shear stress over the surface of the membrane in the feed side for Re = 300, 800 and 1500, respectively. The shear stress is normalized with the maximum value of the shear stress for each case. Shear stress plays an important role in assessing membrane performance as it is a measure of the propensity of fouling over the membrane surface. For small spacer strand diameters, the shear stress distribution over the membrane surface acts like an empty channel case. Only the region near the strands has low value of shear stress. It is these regions were fouling is more prone to happen. As flow rate is increased, the regions of low shear stress near the strands get larger. As the spacer strand diameter is increased to 0.2*h*, the distribution has changed compared to 0.1*h*. For Re = 300, the shear stress distribution is almost constant, However, near the strands, some variations are observed. For Re = 800, the distribution changes and near the intersection of the strands the fouling starts to decrease and creating a split region of high shear stress. The shear stress distribution is clear in Re = 1500, where each spacer cell contains two distinct high shear stress regions. It is observed that behind the intersection of strands there is a very low shear stress region. Fouling is more prone to regions of low shear stress. The effect of increasing the spacers strand diameter to D = 0.3*h* on the shear stress is clear form Fig. 30 (c1, c2, c3). For Re = 300, the regions behind the strands in the flow direction is a low shear stress region. Fouling is prone to accumulate in this region. However, the small flow rate is making the regions of high shear stress larger. In Re = 800, as the flow rate is increased the region of low shear stress gets larger. The low shear stress region starts to grow and bisect the large shear stress region observed in Re = 300 into two regions. For the largest flow rate, Re = 1500, the distribution of the shear stress becomes more uneven. Both high and low shear stress regions are present. Table 11 shows the maximum shear stress values over the feed membrane.

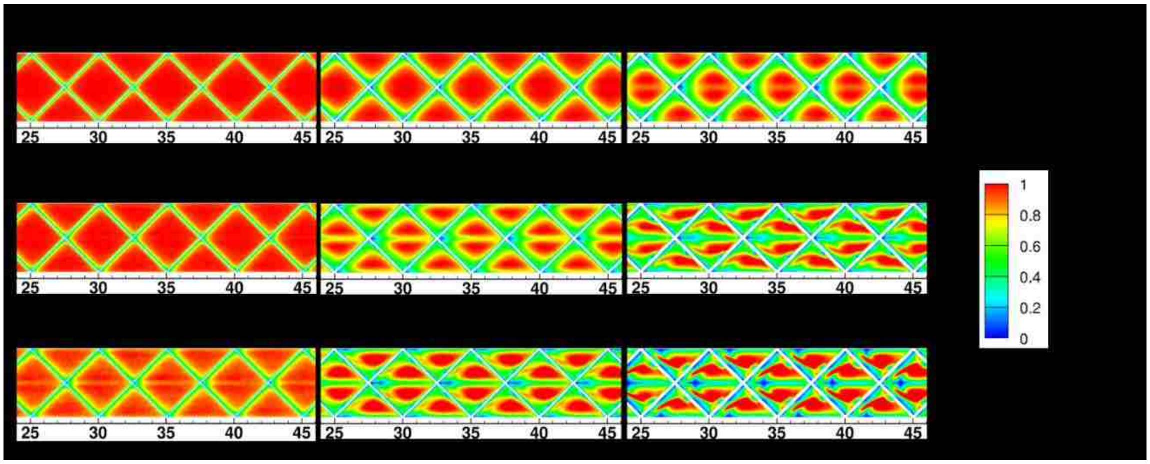

Figure 30. *Normalized shear stress over the membrane surface in the feed side for Re = 300 (a1, b1, c1), Re = 800 (a2, b2, c2), Re = 1500 (a3, b3, c3).*

Table 11. Maximum shear stress values over the membrane surface in the feed channel – all values are in the unit of Pa

Re	**Case**		
	D = 0.1*h*	**D = 0.2*h***	**D = 0.3*h***
300	**1.05**	**1.07**	**1.09**
800	**3**	**3.1**	**3.49**
1500	**6.75**	**7.1**	**12.5**

Fig. 31 (a, b, c) shows the normalized local water flux over the membrane surface in the draw side for Re = 300, 800 and 1500, respectively. The water flux is normalized with the pure water permeability and the osmotic transmembrane pressure. For Re = 300, the water flux has a constant distribution over the membrane surface. At this flow rate with spacer strand diameter of D = 0.1 *h*, no improvement in water flux is observed. As the flow rate is increased, the water flux starts to improve in the regions away from the strands intersections. By comparing Fig. 31 results with the concentration contours in Fig 27 and 28, it is clear that low values of water flux coincide with high and low concentration regions in the feed and draw sides of the membrane, respectively. For D = 0.2*h*, the water flux at Re = 300 did not improve much. However, the distribution of the water flux indicates that there is little increase. For Re = 800, the distribution became more distinct, and the low water flux regions corresponds to low shear stress and high feed concentration. As for Re = 1500, higher value of water flux is observed. Again, the region behind the strand's intersection corresponds to a low water flux region, and it is expected that fouling will be present in these regions. For D = 0.3h and Re = 300, marginal improvement is seen in the water flux. The middle region near the intersection of each strand corresponds to a low water flux region. For Re = 800, the increase in the water flux is observed. The low water flux region is the same as Re = 300. However, it is shrinking in size. Similar trend is seen in Re = 1500 with some marginal improvement in the water flux, and the low water flux region started to diminish. Table 12 list the averaged water flux over the membrane surface for all strand's diameters and flow rates.

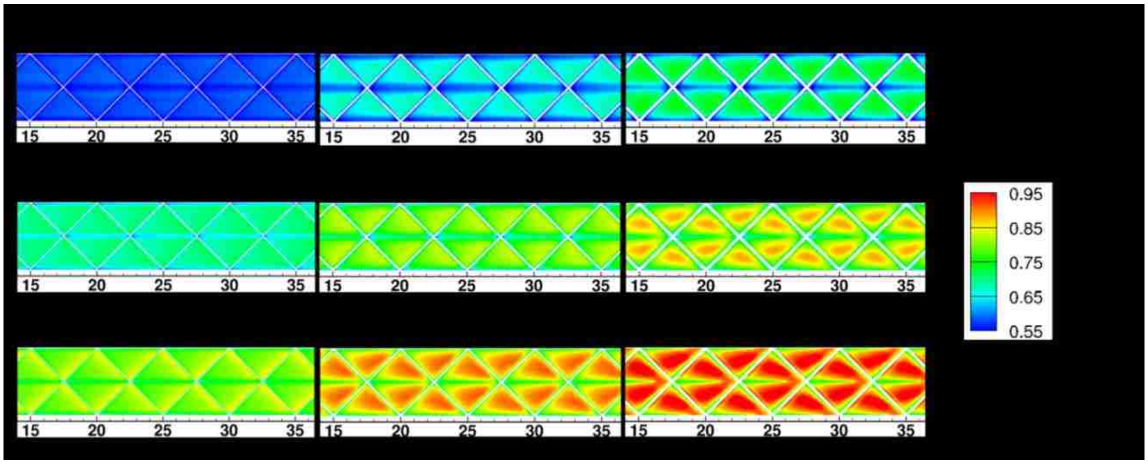

Figure 31. *Normalized water flux for Re = 300 (a1, b1, c1), Re = 800 (a2, b2, c2), Re = 1500 (a3, b3, c3).*

Table 12. Averaged water flux and percentage enhancement for all geometries

	Case											
	Flat			**D = 0.1h**			**D = 0.2h**			**D = 0.3h**		
Re	**300**	**800**	**1500**	**300**	**800**	**1500**	**300**	**800**	**1500**	**300**	**800**	**1500**
Flux $[kg/m^2h]$	50.19	57.93	62.97	55.31	65.45	75.04	60.2	72.70	79.36	63.90	75.16	82.15
Enhancement %	-	-	-	10.20	12.98	19.17	19.94	25.50	26.03	27.32	29.74	30.46

Coefficient of Performance

Although, the enhancements seen in the water flux is quite good. A more detailed analysis is needed to conclude which is the best case. Since the introduction of the embedded spacer will add more friction inside the membrane channels. Therefore, more pumping power is needed to push the feed and draw solution is required. The coefficient of performance parameter is used to estimate which case performed better, and it is written as

$$COP = \left(\frac{J_{ws}}{J_{we}}\right)\left(\frac{\left(f_f+f_d\right)_e}{\left(f_f+f_d\right)_c}\right)^{1/3} \tag{27}$$

where J_{ws} and J_{we} are the averaged water flux for the case with spacer and empty channel, respectively. Also, f_f and f_d are the averaged friction factor for the feed and draw channels, respectively. The subscripts e and s denote to empty and spacer. The friction factor in either side of the channel is calculated using the following relation

$$f = \frac{2\,h\,\left|\frac{dp}{dx}\right|}{0.5\,\rho\,U_{ave}^2} \tag{28}$$

where $\left|\frac{dp}{dx}\right|$ is the pressure gradient in the stream-wise direction. Table 13 lists all the friction values in both channels along with the COP. All the cases presented have a COP value of over 1. This means that the use of embedded spacers helps in getting larger water flux with no severe penalty of pumping power. The case with D = 0.3h and Re =

300 has a COP of 1.20 which is the highest value among all the cases. Two cases of D = 0.1*h* and Re = 300 with D = 0.3*h* and Re = 1500 have a lowest COP value of 1.08. Also, for low flow rate, it is better to use larger strand diameter. Whereas, for higher flow rate, the use of lower strand diameter is recommended.

Table 13. Average friction factor for both the feed and the draw channels and the coefficient of performance for all diameters

Re	Case										
	Empty		D = 0.1*h*			D = 0.2*h*			D = 0.3*h*		
	f_f	f_d	f_f	f_d	COP	f_f	f_d	COP	f_f	f_d	COP
300	**0.26**	**0.27**	**0.27**	**0.28**	**1.08**	**0.29**	**0.30**	**1.15**	**0.31**	**0.32**	**1.20**
800	**0.11**	**0.11**	**0.12**	**0.13**	**1.09**	**0.13**	**0.13**	**1.19**	**0.15**	**0.16**	**1.17**
1500	**0.07**	**0.07**	**0.08**	**0.08**	**1.14**	**0.09**	**0.09**	**1.16**	**0.12**	**0.13**	**1.08**

Conclusion

This chapter focusses on studying forward osmosis membrane systems containing embedded spacers. One of the assumptions made is to eliminate the effect of the porous support layer in the membrane. Therefore, the embedded spacer works as a mixing tool and a support for the membrane. The simulation was conducted using Ansys fluent with the use of user defined function capability. A net-type spacer of 45° was used with three different strand diameters, 0.1*h*, 0.2*h*, and 0.3*h*. Also, the flow rate was varied with three Reynolds numbers of 300, 800, and 1500. Three empty channel cases were simulated as base cases to compare the performance of the embedded spacer approach. The shear stress transport $k - \omega$ model was used for the cases with embedded spacer while a laminar model was employed for the empty channels. The solution-diffusion model was used to predict the water flux over the membrane surface with no modification since the porous layer effect was neglected. All the simulations were conducted with a mesh of 20 million elements based on the mesh optimization test conducted in the previous chapter. The model was also validated in the previous two chapters with empty channels and channels containing mixing promoters.

The results of the simulation were used to characterize the flow in forward osmosis membrane systems containing embedded spacers. The results show that embedded spacers indeed have promoted mixing. Both concentrative and dilutive CP were alleviated in both sides of the membrane. Also, the embedded spacers increased the shear stress over the membrane surface in the feed side. The increase in the shear stress helps in lowering the chances of fouling over the membrane surface as fouling occurs in regions of low shear stress. As expected, the highest water flux occurred at D = 0.3h and Re = 1500 while the lowest water flux occurred at D = 0.1h and Re = 300. However, a coefficient of performance analysis reveals that the case with D = 0.3h and Re = 300 has performed better compared to all the cases. Two cases with D = 0.1h and Re = 300 and with D = 0.3h and Re = 1500 had the lowest performance.

The results show a promising performance for the embedded-spacer concept in forward osmosis desalination modules. It is recommended that more optimization is needed to reach to an optimum embedded-spacer arrangement as there is an endless ways of spacer arrangements.

Chapter 6: Conclusion

In this work, water desalination based on forward osmosis membrane systems is studied. Computational fluid dynamic (CFD) tools are utilized to simulate such systems. There are several commercial and open source CFD tools available today such as COMSOL, FLUENT, CFX, Star-CCM+, OpenFOAM, Autodesk, and many others. The simulations in this work were conducted using Ansys Fluent software. There are several steps needed to conduct CFD simulations. The following graph shows a simple diagram for the flow process of any CFD simulation.

Figure 32. *General stages of any CFD simulation.*

In the pre-processing step, the computational domain is constructed. If the computational domain is of simple structure, it can be constructed using text commands that provide coordinates of the domain. With complicated computational domains, Ansys design modeler can be utilized or any other CAD software such as SolidWorks. After defining the required domain, the domain needs to be discretized. This can be done using Ansys meshing tool. For the empty channel case considered in chapter 3, a structured mesh was used for the simplicity of the domain. However, in the corrugated membrane and the embedded membrane cases presented in chapter 4 and 5, respectively, an unstructured mesh was utilized since the geometry became complicated. Therefore, different methods of meshing can be utilized depending on the computational domain.

In the processing step, the governing equations are solved using Ansys Fluent. So, for the simulations considered in this work, NaCl was used as both the feed and draw solutions with different concentrations. The properties of the solution are entered using Ansys Fluent. As for the flux equation described in the mathematical model along with the membrane boundary conditions. The use of User Defined Functions (UDF) was utilized. The UDF is a C file that can be written in a text document and then be compiled to Fluent so that the membrane boundary conditions can be entered in Fluent. UDF is a powerful tool to be used to customize any boundary conditions needed in Fluent. Then, the governing equations can be coupled with the membrane boundary conditions, and the solution procedure is initiated.

In the post-processing step, the solution file is taken from Fluent and exported to CFD-post, or sometimes the post-processing is done in Fluent its self. In CFD-post several capabilities are available that can give the user the power to produce the required plots or contours and any required result from the Fluent file. These results can then be exported to any other software for further post-processing or can be taken directly.

In Forward osmosis desalination systems, sea or brackish water is placed in one channel. A draw solution with a concentration higher than the sea or the brackish water is introduced in another channel. The two channels are separated by a semi-permeable membrane. The membrane acts as a barrier to salt ions and particulate. Only water molecules are allowed to pass. The driving force of the water permeation is the concentration difference across the membrane. As the seawater continues to flow in the channel, its concentration increases due to the passage of water to the draw channel. Within the other channel, the draw solution losses concentration as it flows down-stream.

Since changes in concentration in both channels are local near the membrane surface that will create polarization known as the external concentration polarization. Concentration polarization has an adverse effect on the performance of forward osmosis systems.

When looking at the structure of any forward osmosis membrane, a dense active layer is supported by a porous support layer. The porous support layer is needed to give the active layer the necessary mechanical support for a longer operational time. However, the existence of the porous support layer give rise to a phenomenon called internal concentration polarization. Depending on the orientation of the membrane, the internal concentration polarization could be either concentrative or dilutive. In desalination with forward osmosis, it is preferred to orient the porous support layer to the draw side so that no salt build-up can happen inside the porous layer. Therefore, only internal dilutive concentration polarization is present in this orientation.

Since the driving force in forward osmosis is the concentration difference between the feed and the draw solutions, the concentration of the feed needs to be as low as possible, and the concentration of the draw solution needs to be as high as possible. However, this is hindered by the external and internal concentration polarization effects. To avoid such effects, the concentration polarization needs to be mitigated. The simplest way is to increase the flow rate of both the feed and draw solutions. This can lead to a reduction in the concentration boundary layer and therefore an increase in the water permeation rate. Another method is to use mixing promoters inside the channels. Mixing promoters are solid structures that can be placed inside the channels as passive control systems. Usually, they have two main functions. The first is to enhance mixing and disrupt the growth of the concentration boundary layer. The second is to add extra mechanical support for the membrane. However, mixing promoters add an extra pressure loss to the system.

The main objectives of this Ph.D. dissertation were to investigate the following:

1- The effect of porous layer thickness and operation parameters on FO system performance
2- The effect of membrane and channel corrugation on water flux enhancement
3- The effect of embedded spacer on water flux enhancement and mitigating concentration polarization

Each of these objectives was studied in full details in chapters 3, 4, and 5, respectively.

Before the simulations were conducted, a mesh optimization test was done on every geometry used. The mesh optimization tests revealed that the element number of mesh is 20 million for the corrugated and the embedded spacer cases. The mesh for the empty channel was only 2 million elements.

Also, the mathematical model was validated several times. The first validation was done on an empty channel with the effect of the porous support layer. The second validation was conducted with the inclusion of the net-type spacers of 45° in the middle of the feed and the draw channels. The third set of the validations was for an empty channel without the effect of the porous layer support. A good agreement with the results obtained from the mathematical model and the experiments was achieved.

In the first objective, three-dimensional empty channels were constructed and modeled. The membrane was treated as a functional surface of zero thickness. The porous layer effect was included in the flux equation where a modified version of the solution-diffusion equation was used. The distribution of the velocity and concentration fields were obtained everywhere in the channels. It was shown in the results that increasing the flow rate indeed improved the performance of forward osmosis systems when the thickness of the porous layer was small. Also, the water permeation is higher at the inlet of the draw channel then; it starts to decrease along the draw channel. Near the draw outlet the water permeation rate starts to increase due to the effect of the low concentrated feed entering in the feed channel. It was also shown that by increasing the porous layer thickness from 50 to 110 μm, the water flux decreased by 56%. So, increasing the flow rate of both streams at thicker porous layer thickness will not have any significant effect on the water flux improvement.

In the second objective, membrane and channel corrugations were modeled. Three empty channels cases with Re = 300, 800, and 1500 were used as base cases. Triangular corrugation was used as a mixing promoter. In this kind of corrugation, the membrane is corrugated in two different ways; the first is a single triangular corrugation while the second is a double triangular corrugation. In the single corrugation, the peaks of the corrugation are pointed towards the feed channel. This was done to mitigate salt built-up in the feed channel and to avoid fouling. The double triangular corrugation gives peaks in both sides of the channel and dips in both channels as well. Also, channel corrugation is considered. In this configuration, the membrane is not corrugated. Only the channel walls are corrugated. It is to be noted that the corrugation is of chevron type. This kind of corrugation gives good mixing with lower pressure drop. Our results show that corrugation gave good mixing in both channels except the draw channel in the single corrugation case since only dips are present in the draw side. The corrugation also helped in reducing both dilutive and concentrative external concentration polarization. Corrugation will help in reducing the fouling over the membrane surface since high shear stress regions were seen over the membrane surface in the feed channel. The combined case with Re = 1500 had the highest water flux where the channel corrugation with Re = 300 had the lowest water flux. When looking at the coefficient of performance, the single and double corrugation cases with Re = 300 had the highest value of COP. The combined corrugation case with Re = 1500 had the lowest value of COP.

The third objective looked at the effect of embedded spacers in forward osmosis membrane systems. One of the main assumptions made in this chapter was to eliminate the effect of the porous support layer in the membrane. The embedded spacers will work as mechanical support for the membrane, and it will be considered as a mixing promoter. Three different values of Reynolds number were considered as 300, 800, and 1500. The results were compared with base cases (empty channels) for the same flow rates. The embedded spacer considered was a net-type spacer of 45°. The strands diameter was changed as 0.1h, 0.2h, and 0.3h where h is the height of the feed and draw channel. The solution-diffusion model was used to describe the flux through the membrane without any modification since the effect of the porous support layer was eliminated. The results show that embedded spacers have induced mixing inside the channels. The external concentrative or dilutive concentration polarization was also alleviated. High shear stress regions were observed over the membrane surface. The higher the shear stress is the better since this will reduce the chance of fouling occurrence over the membrane surface in the feed channel. The highest water flux obtained was in the case with D = 0.3h and Re = 1500 while the lowest water flux was with the case with D = 0.1h and Re = 300.

However, the coefficient of performance analysis shows that the case with D = 0.3h and Re = 300 had the best performance.

The current mathematical model could also be applied to several other forward osmosis configurations. One such configuration is hollow fiber systems. In hollow fiber systems, the feed could be introduced inside the hollow fibers and the draw solution can be outside the hollow fibers or vice versa. The hollow fibers could also be twisted or modified in any way such that external polarization could be mitigated.

It was shown in chapter 3 that the porous support layer has an adverse effect on the performance on forward osmosis systems. It was also shown that when the porous layer was eliminated the system performed better. So, a detailed study could be spent on investigating the flow inside the pores of the porous layer. This could be achieved by studying the flow in a molecular dynamic scale. This kind of analysis will give a great insight on how forward osmosis membranes can be designed.

The mathematical model could also be used to study the natural osmosis phenomenon that takes place in natural living organisms such as plant roots or the human body. Dialyses could be investigated and improved further in a similar fashion to forward osmosis.

References

[1] J.L. Ivey, J. Smithers, R.C. De Loë, R.D. Kreutzwiser, Community Capacity for Adaptation to Climate-Induced Water Shortages: Linking Institutional Complexity and Local Actors, Environ. Manage. 33 (2004) 36–47. doi:10.1007/s00267-003-0014-5.

[2] Guidelines for Drinking-water Quality, (2011) 1–23. doi:10.1017/CBO9781107415324.004.

[3] E. Drioli, Guest Editorial for the Special Issue: Membrane Distillation and related Membrane Systems, Desalination. 323 (2013) 1. doi:10.1016/j.desal.2013.02.015.

[4] A. Pérez-González, A.M. Urtiaga, R. Ibáñez, I. Ortiz, State of the art and review on the treatment technologies of water reverse osmosis concentrates, Water Res. 46 (2012) 267–283. doi:10.1016/j.watres.2011.10.046.

[5] H.T. El-Dessouky, H.M. Ettouney, Y. Al-Roumi, Multi-stage flash desalination: Present and future outlook, Chem. Eng. J. 73 (1999) 173–190. doi:10.1016/S1385-8947(99)00035-2.

[6] A. Alkhudhiri, N. Darwish, N. Hilal, Membrane distillation: A comprehensive review, Desalination. 287 (2012) 2–18. doi:10.1016/j.desal.2011.08.027.

[7] J. a Baker, Menbrane Technology and Applications, Q. Rev. Biol. 79 (2004) 443. doi:10.1086/428225.

[8] Z. Cao, D.E. Wiley, A.G. Fane, CFD simulations of net-type turbulence promoters in a narrow channel, J. Memb. Sci. 185 (2001) 157–176. doi:10.1016/S0376-7388(00)00643-8.

[9] S. Wardeh, H.P. Morvan, CFD simulations of flow and concentration polarization in spacer-filled channels for application to water desalination, Chem. Eng. Res. Des. 86 (2008) 1107–1116. doi:10.1016/j.cherd.2008.04.010.

[10] O. Kavianipour, G.D. Ingram, H.B. Vuthaluru, Investigation into the effectiveness of feed spacer configurations for reverse osmosis membrane modules using Computational Fluid Dynamics, J. Memb. Sci. 526 (2017) 156–171. doi:10.1016/j.memsci.2016.12.034.

[11] T. Cath, A. Childress, M. Elimelech, Forward osmosis: Principles, applications, and recent developments, J. Memb. Sci. 281 (2006) 70–87. doi:10.1016/j.memsci.2006.05.048.

[12] M.F. Gruber, C.J. Johnson, C.Y. Tang, M.H. Jensen, L. Yde, C. Hélix-Nielsen, Computational fluid dynamics simulations of flow and concentration polarization in forward osmosis membrane systems, J. Memb. Sci. 379 (2011) 488–495. doi:10.1016/j.memsci.2011.06.022.

[13] A.H. Hawari, N. Kamal, A. Altaee, Combined influence of temperature and flow rate of feeds on the performance of forward osmosis, Desalination. 398 (2016) 98–105. doi:10.1016/j.desal.2016.07.023.

[14] H. Zhang, S. Cheng, F. Yang, Use of a spacer to mitigate concentration polarization during forward osmosis process, Desalination. 347 (2014) 112–119. doi:10.1016/j.desal.2014.05.026.

[15] A.E. Anqi, N. Alkhamis, A. Oztekin, Numerical simulation of brackish water desalination by a reverse osmosis membrane, Desalination. 369 (2015) 156–164. doi:10.1016/j.desal.2015.05.007.

[16] A.E. Anqi, N. Alkhamis, A. Oztekin, Steady three dimensional flow and mass transfer analyses for brackish water desalination by reverse osmosis membranes, Int. J. Heat Mass Transf. 101 (2016) 399–411. doi:https://doi.org/10.1016/j.ijheatmasstransfer.2016.05.102.

[17] M. Usta, A.E. Anqi, A. Oztekin, Reverse osmosis desalination modules containing corrugated membranes – Computational study, Desalination. 416 (2017) 129–139. doi:https://doi.org/10.1016/j.desal.2017.05.005.

[18] J. Wei, C. Qiu, C.Y. Tang, R. Wang, A.G. Fane, Synthesis and characterization of flat-sheet thin film composite forward osmosis membranes, J. Memb. Sci. 372 (2011) 292–302. doi:https://doi.org/10.1016/j.memsci.2011.02.013.

[19] G. Han, T.-S. Chung, M. Toriida, S. Tamai, Thin-film composite forward osmosis membranes with novel hydrophilic supports for desalination, J. Memb. Sci. 423–424 (2012) 543–555. doi:https://doi.org/10.1016/j.memsci.2012.09.005.

[20] M.F. Gruber, U. Aslak, C. Hélix-Nielsen, Open-source CFD model for optimization of forward osmosis and reverse osmosis membrane modules, Sep. Purif. Technol. 158 (2016) 183–192. doi:10.1016/j.seppur.2015.12.017.

[21] M. Park, J.H. Kim, Numerical analysis of spacer impacts on forward osmosis membrane process using concentration polarization index, J. Memb. Sci. 427 (2013) 10–20. doi:10.1016/j.memsci.2012.09.045.

[22] P. Liu, H. Zhang, Y. Feng, C. Shen, F. Yang, Influence of spacer on rejection of trace antibiotics in wastewater during forward osmosis process, Desalination. 371 (2015) 134–143. doi:10.1016/j.desal.2015.06.006.

[23] R. Valladares Linares, S.S. Bucs, Z. Li, M. AbuGhdeeb, G. Amy, J.S. Vrouwenvelder, Impact of spacer thickness on biofouling in forward osmosis, Water Res. 57 (2014) 223–233. doi:10.1016/j.watres.2014.03.046.

[24] N. Tzanetakis, W.M. Taama, K. Scott, R.J.J. Jachuck, The effect of corrugated membranes

on salt splitting, J. Appl. Electrochem. 33 (2003) 411–417. doi:10.1023/A:1024428106739.

[25] K. Scott, R.J. Jachuck, D. Hall, Crossflow microfiltration of water-in-oil emulsions using corrugated membranes, Sep. Purif. Technol. 22–23 (2001) 431–441. doi:10.1016/S1383-5866(00)00180-5.

[26] X. Song, Z. Liu, D.D. Sun, Nano Gives the Answer: Breaking the Bottleneck of Internal Concentration Polarization with a Nanofiber Composite Forward Osmosis Membrane for a High Water Production Rate, Adv. Mater. 23 (2011) 3256–3260. doi:10.1002/adma.201100510.

[27] J. Marc, C. Puguan, H. Kim, K. Lee, H. Kim, Low internal concentration polarization in forward osmosis membranes with hydrophilic crosslinked PVA nano fibers as porous support layer, Desalination. 336 (2014) 24–31. doi:10.1016/j.desal.2013.12.031.

[28] M. Ghanbari, D. Emadzadeh, W.J. Lau, H. Riazi, D. Almasi, A.F. Ismail, Minimizing structural parameter of thin film composite forward osmosis membranes using polysulfone / halloysite nanotubes as membrane substrates, Desalination. 377 (2016) 152–162. doi:10.1016/j.desal.2015.09.019.

[29] W. Kuang, Z. Liu, H. Yu, G. Kang, X. Jie, Y. Jin, Y. Cao, Investigation of internal concentration polarization reduction in forward osmosis membrane using nano-CaCO 3 particles as sacrificial component, J. Memb. Sci. 497 (2016) 485–493. doi:10.1016/j.memsci.2015.06.052.

[30] N. Bui, J.R. Mccutcheon, Nanoparticle-embedded nanofibers in highly permselective thin-film nanocomposite membranes for forward osmosis, J. Memb. Sci. 518 (2016)

338–346. doi:10.1016/j.memsci.2016.06.024.

[31] M. Li, V. Karanikola, X. Zhang, L. Wang, M. Elimelech, A Self-Standing, Support-Free Membrane for Forward Osmosis with No Internal Concentration Polarization, Environ. Sci. Technol. Lett. 5 (2018) 266–271. doi:10.1021/acs.estlett.8b00117.

[32] V. Geraldes, V. Semião, M.N. De Pinho, Flow and mass transfer modelling of nanofiltration, J. Memb. Sci. 191 (2001) 109–128. doi:10.1016/S0376-7388(01)00458-6.

[33] S. Loeb, L. Titelman, E. Korngold, J. Freiman, Effect of porous support fabric on osmosis through a Loeb-Sourirajan type asymmetric membrane, J. Memb. Sci. 129 (1997) 243–249. doi:10.1016/S0376-7388(96)00354-7.

[34] A. Tiraferri, N.Y. Yip, W.A. Phillip, J.D. Schiffman, M. Elimelech, Relating performance of thin-film composite forward osmosis membranes to support layer formation and structure, J. Memb. Sci. 367 (2011) 340–352. doi:10.1016/J.MEMSCI.2010.11.014.

[35] S. Soukane, M.W. Naceur, L. Francis, A. Alsaadi, N. Ghaffour, Effect of feed flow pattern on the distribution of permeate fluxes in desalination by direct contact membrane distillation, Desalination. 418 (2017) 43–59. doi:10.1016/j.desal.2017.05.028.

[36] N.Y. Yip, A. Tiraferri, W.A. Phillip, J.D. Schiffman, M. Elimelech, High Performance Thin-Film Composite Forward Osmosis Membrane, Environ. Sci. Technol. 44 (2010) 3812–3818.

[37] G.T. Gray, J.R. McCutcheon, M. Elimelech, Internal concentration polarization in forward osmosis: role of membrane orientation, Desalination. 197 (2006) 1–8. doi:10.1016/j.desal.2006.02.003.

[38] H.Q. Liang, W.S. Hung, H.H. Yu, C.C. Hu, K.R. Lee, J.Y. Lai, Z.K. Xu, Forward osmosis

membranes with unprecedented water flux, J. Memb. Sci. 529 (2017) 47–54. doi:10.1016/j.memsci.2017.01.056.

[39] M. Qasim, N.A. Darwish, S. Sarp, N. Hilal, Water desalination by forward (direct) osmosis phenomenon: A comprehensive review, Desalination. 374 (2015) 47–69. doi:10.1016/j.desal.2015.07.016.

[40] A.E. Anqi, N. Alkhamis, A. Oztekin, Computational study of desalination by reverse osmosis — Three-dimensional analyses, Desalination. 388 (2016) 38–49. doi:https://doi.org/10.1016/j.desal.2016.03.017.

Appendix A: Source Code for the User Defined Function

```
#include "udf.h"
#include "mem.h"
#include "math.h"
#include "stdio.h"
#include"stdlib.h"
#include <ctype.h>
#include <string.h>
#define Per 3.08e-12   /* Pure water membrane permeability */
#define B 1.27e-7    /* membrane solute permeability */
#define phi 805.0e2 /* propotionilaty factor */
#define Pc 80510000.00 /* coffeient of ma */
/*#define ep 0.25 /* porosity of membrane porous support
#define del 8.6e-5 /* porous layer thickness
tao = 1.0 - 0.8*log(ep) = 2.11
K =483672.14
*/
#define K 346599.1
int CheckSign(real a)
{
int CS;

if(a>0){

CS = 1;
    return CS;
}
else if(a<0){
```

```
CS = -1;
      return CS;
}
else{

CS = 0;
      return CS;
}


}
real FluxW(real Jw, real piF, real piD)
{
real Num = B + (Per*piD*Pc);
real Den = B + fabs(Jw) + (Per*piF*Pc);
if (Den > 1e-15){
   return ( Jw - ( (1.0/K) * log(Num/Den) ) );
}
else{
   return 0;
}
}
  real FluxS(real Jw)
{
return (-B/(phi*Per))* Jw;
}
real Ridder(real piF,real piD,real minBound,real maxBound ,real xacc)
{
real xnew=0.0;
real fl = FluxW(minBound, piF, piD);
```

```
real fh = FluxW(maxBound, piF, piD);
if( (fl > 0.0 && fh < 0.0) || (fl < 0.0 && fh > 0.0) )
{
real xl = 0.0;
real xh = 0.1;
real ans1 = -1.1e-30;
int j;
for(j=0; j < 50; j++)
{
   real xm = (xl+xh)/2.0;
   real fm = FluxW(xm, piF, piD);
   real s=sqrt( (fm*fm) - (fl*fh));
   if ( s < 1.0e-15 ) {
     return ans1;
   }
   if (fl >= fh){
      xnew = xm + (xm-xl)*fm/s;
             }
   else{
      xnew = xm - (xm-xl)*fm/s;
       }
   if (fabs(xnew-ans1) <= xacc) {
     return ans1;
   }
   ans1 = xnew;
   real fnew = FluxW(ans1, piF, piD);
   if ( fabs(fnew) < 1.0e-15) {
    return ans1;
   }
```

```
    if (CheckSign(fm) != CheckSign(fnew)){
            xl = xm;
            xh = fm;
            fl = ans1;
            fh = fnew;
     }
    else if (CheckSign(fl) != CheckSign(fnew)){
        xh = ans1;
        fh = fnew;
     }
    else if(CheckSign(fh) != CheckSign(fnew)){
        xl = ans1;
        fl=fnew;
     }
    else{
          printf("Error");
       return 0;
       }
} /* for for */
}
else if(fabs(fl) < 1.0e-15){
        return minBound;
}
else{
        return maxBound;
}
return 0;
}
DEFINE_PROFILE(FeedGradient, t, i)
```

```
{
        face_t f;
        Thread *Bc,*Dc;
        Thread *tf1;
        cell_t c0,c1;
        real Jw, Js;
    if (! Data_Valid_P())
      return;
        Bc=THREAD_T0(t); tf1=THREAD_SHADOW(t); Dc=THREAD_T0(tf1);
        begin_f_loop(f, t)
        {
                c0=F_C0(f,t);      c1=F_C0(f,tf1);
                        Jw = Ridder(C_UDSI(c0,Bc,0), C_UDSI(c1,Dc,0), 0.0, 0.1 , 1.0e-15);
                        Js = FluxS(Jw);
                F_PROFILE(f, t, i) = (-Js + Jw*C_UDSI(c0,Bc,0)*C_R(c0,Bc));
        }
        end_f_loop(f, t)
}
DEFINE_PROFILE(DrawGradient, t, i)
{
        face_t f;
        Thread *Bc,*Dc;
        Thread *tf1;
        cell_t c0,c1;
        real Jw1, Js1;
    if (! Data_Valid_P())
      return;
        Bc=THREAD_T0(t); tf1=THREAD_SHADOW(t); Dc=THREAD_T0(tf1);
        begin_f_loop(f, t)
```

```
    {
        c0=F_C0(f,t);      c1=F_C0(f,tf1);
            Jw1 = Ridder(C_UDSI(c1,Dc,0), C_UDSI(c0,Bc,0), 0.0, 0.1, 1.0e-15);
            Js1 = FluxS(Jw1);
        F_PROFILE(f, t, i) =  (Js1- Jw1*C_UDSI(c0,Bc,0)*C_R(c0,Bc) );
    }
    end_f_loop(f, t)
}
DEFINE_PROFILE(SuctionVelocity, t, i)
{
    face_t f;
    Thread *Bc,*Dc;
    Thread *tf1;
    cell_t c0,c1;
    real Jw2;
  if (! Data_Valid_P())
   return;
    Bc=THREAD_T0(t); tf1=THREAD_SHADOW(t); Dc=THREAD_T0(tf1);
    begin_f_loop(f, t)
    {
        c0=F_C0(f,t);      c1=F_C0(f,tf1);
            Jw2 = Ridder(C_UDSI(c0,Bc,0), C_UDSI(c1,Dc,0), 0.0, 0.1, 1.0e-15);
        F_PROFILE(f, t, i) = Jw2;
    }
    end_f_loop(f, t)
}
DEFINE_PROFILE(BlowVelocity, t, i)
{
    face_t f;
```

```
    Thread *Bc,*Dc;

    Thread *tf1;

    cell_t c0,c1;

    real Jw3;

  if (! Data_Valid_P())

   return;

    Bc=THREAD_T0(t); tf1=THREAD_SHADOW(t); Dc=THREAD_T0(tf1);

    begin_f_loop(f, t)

    {

        c0=F_C0(f,t);      c1=F_C0(f,tf1);

                Jw3 = Ridder(C_UDSI(c1,Dc,0), C_UDSI(c0,Bc,0), 0.0, 0.1, 1.0e-15);

        F_PROFILE(f, t, i) = Jw3 * (C_R(c0,Bc)/C_R(c1,Dc));

    }

    end_f_loop(f, t)

}

DEFINE_PROFILE(inlet_Feed_Velocity, thread, nv)

{

real x[3];

real y;

real hi = 0.001;

real Uav = 0.3;

face_t f;

begin_f_loop(f, thread)

{

    F_CENTROID(x,f,thread);

    y= x[1];

    F_PROFILE(f, thread, nv)

        = 6.*Uav*(y/hi)*( (1.-(y/hi)) );

}
```

```
end_f_loop(f, thread)
}
DEFINE_PROFILE(inlet_Draw_Velocity, thread, nv)
{
real x[3];
real y;
real hi = 0.001;
real Uav = 0.3;
face_t f;
begin_f_loop(f, thread)
{
      F_CENTROID(x,f,thread);
      y= x[1];
      F_PROFILE(f, thread, nv)
            = -6.*Uav*((y-0.001)/hi)*( (1.-(y-0.001)/hi) );
}
end_f_loop(f, thread)
}
DEFINE_PROPERTY(cell_viscosity,cell,thread)
 {
   real mu_lam;
   real index;
   if (! Data_Valid_P())
     return;
   real m_A = C_UDSI(cell,thread,index);
     mu_lam = 0.00089*(1.+1.63*m_A);
   return mu_lam;
}
DEFINE_PROPERTY(cell_density,cell,thread)
```

```
 {
   real rho_lam;
   real index;
   if (! Data_Valid_P())
     return;
   real m_A = C_UDSI(cell,thread,index);
     rho_lam = 997.1+694*m_A;
   return rho_lam;
}
DEFINE_DIFFUSIVITY(cell_diff,cell,thread,index)
 {
   real dif_lam;
   if (! Data_Valid_P())
     return;
     dif_lam = MAX((0.00000000161*(1-
(14*C_UDSI(cell,thread,index))))*C_R(cell,thread),(0.00000000145)*C_R(cell,thread));
   return dif_lam;
}
```

VITA

Ahmed Alshwairekh was born on Augest 7 – 1987 in Buraydah Saudi Arabia. Ahmed joined the college on Engineering at Qassim University in 2005 and graduated from the Mechanical Engineering Department with the second-class honor in July 2009. Shortly after graduation, Ahmed started working at the Mechanical Engineering Dept. at Qassim University as a teaching assistant. He taught several lab courses such as fluid mechanics lab, thermodynamics, and heat transfer lab. In August 2011, Ahmed joined the Mechanical Engineering Department at the University of Dayton as a master's student. He graduated in May 2013 and returned to work for two years in Qassim University in Saudi Arabia as a lecturer. During this time Ahmed assisted several professors with their courses such as the course titled selected topics "Indoor Air Quality and Introduction to Academic Research". Ahmed joined Lehigh University in 2016 for his PhD studies and started working with the "membrane group" under the supervision of Professor Alparslan Oztekin. The title of Ahmed's PhD dissertation is "Computational Study of Water Desalination Using Forward Osmosis".